Monthly Notices
of the
ROYAL ASTRONOMICAL SOCIETY

MNRAS **477,** 2991–3013 (2018) doi:10.1093/mnras/sty723
Advance Access publication 2018 March 17

A VLT/MUSE galaxy survey towards QSO Q1410: looking for a WHIM traced by BLAs in inter-cluster filaments★

Ismael Pessa,[1]† Nicolas Tejos,[2]† L. Felipe Barrientos,[1,3] Jessica Werk,[4] Richard Bielby,[5] Nelson Padilla,[1,6] Simon L. Morris,[5] J. Xavier Prochaska,[7] Sebastian Lopez[8] and Cameron Hummels[9]

[1]*Instituto de Astrofísica, Pontificia Universidad Católica de Chile, Vicuña Mackenna 4860, Santiago, Chile*
[2]*Instituto de Física, Pontificia Universidad Católica de Valparaíso, Casilla 4059, Valparaíso, Chile*
[3]*Millennium Institute of Astrophysics, Santiago, Chile*
[4]*Department of Astronomy, University of Washington, Seattle, WA 98195-1580, USA*
[5]*Department of Physics, Durham University, South Road, Durham DH1 3LE, UK*
[6]*Centro de Astro-Ingeniería, Pontificia Universidad Católica de Chile, Santiago, Chile*
[7]*Department of Astronomy and Astrophysics, UCO/Lick Observatory, University of California, 1156 High Street, Santa Cruz, CA 95064, USA*
[8]*Departamento de Astronomía, Universidad de Chile, Casilla 36-D, Santiago, Chile*
[9]*TAPIR, California Institute of Technology, Pasadena, CA 1125, USA*

Accepted 2018 March 15. Received 2018 March 15; in original form 2017 November 20

ABSTRACT

Cosmological simulations predict that a significant fraction of the low-z baryon budget resides in large-scale filaments in the form of a diffuse plasma at temperatures $T \sim 10^5 - 10^7$ K. However, direct observation of this so-called warm-hot intergalactic medium (WHIM) has been elusive. In the Λcold dark matter paradigm, galaxy clusters correspond to the nodes of the cosmic web at the intersection of several large-scale filamentary threads. In previous work, we used *HST*/COS data to conduct the first survey of broad H I Lyα absorbers (BLAs) potentially produced by WHIM in inter-cluster filaments. We targeted a single QSO, namely Q1410, whose sightline intersects seven independent inter-cluster axes at impact parameters <3 Mpc (comoving), and found a tentative excess of a factor of $\sim$4 with respect to the field. Here, we further investigate the origin of these BLAs by performing a blind galaxy survey within the Q1410 field using VLT/MUSE. We identified 77 sources and obtained the redshifts for 52 of them. Out of the total sample of seven BLAs in inter-cluster axes, we found three *without* any galaxy counterpart to stringent luminosity limits ($\sim 4 \times 10^8\,L_\odot$ $\sim 0.01\,L_*$), providing further evidence that these BLAs may represent genuine WHIM detections. We combined this sample with other suitable BLAs from the literature and inferred the corresponding baryon mean density for these filaments in the range $\Omega_{\rm bar}^{\rm fil} = 0.02 - 0.04$. Our rough estimates are consistent with the predictions from numerical simulations but still subject to large systematic uncertainties, mostly from the adopted geometry, ionization corrections, and density profile.

Key words: methods: observational – techniques: spectroscopic – intergalactic medium – quasars: absorption lines – large-scale structure of Universe.

1 INTRODUCTION

The current cosmological paradigm predicts that only $\sim$4.8 per cent of the energy content in the Universe is in the form of baryonic matter (Planck Collaboration XIII 2016). At higher redshifts ($z \gtrsim 3$) about 90 per cent of the baryons are assembled in the diffuse photoionized intergalactic medium (IGM; Weinberg et al. 1997) that give raise to the so-called Lyα Forest. In contrast, in the local Universe the fraction of baryons in this phase is only $\sim$30 per cent (Penton, Stocke & Shull 2004; Lehner et al. 2007). From the remaining baryons, only $\sim$30–40 per cent are found in other well-studied phases (e.g. stars, ISM, cluster gas) (Davé et al. 2001), leaving $\sim$40–30 per cent of the low-z baryons unaccounted for. This is the so-called missing baryons problem on cosmic scales, where

★Based on observations collected at the European Organization for Astronomical Research in the Southern hemisphere under ESO programme 094.A-0575(C).

†E-mail: ismael.pessa@gmail.com (IP); nicolas.tejos@pucv.cl (NT)

a significant fraction of the total baryons are missing in the $z < 1$ Universe (Persic & Salucci 1992; Fukugita, Hogan & Peebles 1998; Prochaska & Tumlinson 2009; Shull, Smith & Danforth 2012).

Different hydrodynamical cosmological simulations based on Λcold dark matter cosmology have predicted that ∼30−40 per cent of the total baryons at low redshift would be in the warm-hot intergalactic medium (WHIM), at temperatures between 10^5 and 10^7 K particularly residing in diffuse filamentary large-scale structures with a median overdensity of ∼10−30 times the mean density of the Universe (Cen & Ostriker 1999; Davé et al. 2001). This is because at the present epoch, hierarchical structure formation model has had time to produce deeper potential wells where baryonic matter is accreted and heated due to the gravitational shocks produced by its collapse. As a consequence of this shock heating, almost all the hydrogen is ionized (by collisional processes or UV radiation) and only a small fraction remains neutral ($f_{\rm H\,I} \sim 10^{-5}$ in a pure collisional ionization scenario; Sutherland & Dopita 1993; Richter et al. 2004).

The definitive observational confirmation of the WHIM has been elusive because of the low expected column density of H I in the hot gas ($N_{\rm H\,I} \approx 10^{13}$ cm^{-2}; Richter et al. 2006b) and large Doppler parameters (typically $b \geq 40$ km s^{-1}; from thermal and non-thermal processes) that would place the absorption features produced by the WHIM at the limit of detectability (e.g. Cen & Ostriker 1999; Davé et al. 2001). Emission of this plasma is also expected in the UV and X-ray, and marginal detections have been reported (e.g. Hattori et al. 2017); a firm detection in emission still awaits more sensitive telescopes (Fang et al. 2005). More recently, Tanimura et al. (2017) and de Graaff et al. (2017) have reported statistically significant detections ($>5\sigma$) of warm-hot baryons through the thermal Sunyaev–Zel'dovich effect signal in a sample of stacked filaments connecting massive haloes. They established a gas density of approximately six times the mean universal baryon density, accounting for ∼30 per cent of the total baryon budget. However, absorption line techniques may still represent our current best chance to detect *individual* WHIM signatures, particularly through broad H I Lyα absorptions (BLA) in the FUV spectra of bright QSOs.

Previous studies have detected BLAs potentially produced by WHIM at low redshifts (Richter et al. 2006b; Tripp et al. 2006; Lehner et al. 2007; Danforth, Stocke & Shull 2010; Tilton et al. 2012; Wakker et al. 2015). Richter et al. (2006b) calculated the incidence of BLAs per unit redshift to be $dN/dz \approx 22$ using four different QSO sightlines and derived a lower limit for the baryon content of BLAs $\Omega_{\rm BLA} > 0.0027 h_{70}^{-1}$. These results are subject to the uncertainty that not every BLA detected in the FUV QSO spectrum is necessarily related to the WHIM and the authors estimated an associated systematic error as high as 50 per cent, which could lead to an overestimation of $\Omega_{\rm BLA}$. These studies assume collisional ionization equilibrium (CIE), but according to simulations (Fang & Bryan 2001), photoionization by the UV background also becomes important at typical WHIM densities. Neglecting photoionization can conversely lead to underestimation of the baryon density. Bonamente et al. (2016) used *Chandra* spectra and found an absorption line identified as O VIII that could potentially be the X-ray counterpart of the FUV BLA detected by Tilton et al. (2012). Indeed, from the Sloan Digital Sky Survey (SDSS) data Bonamente et al. (2016) found evidence of a large-scale filament structure at nearly the same redshift as the absorption features. Wakker et al. (2015) used *HST* spectra of 24 AGN to sample the gas in a low-z filament, by measuring the properties of 15 Lyα absorbers in the AGN spectra that are likely associated with the intergalactic gas of the filament. In particular, they studied the properties of the gas as a function of the impact parameter to the filament axis and found evidence that the Lyα line-width anticorrelates with the filament impact parameter. Furthermore, the authors found four BLAs in this sample, all of them in the sightlines passing relatively close (<540 kpc) to the axis of the filament, which would suggest an increase in temperature and/or turbulence.

In this paper, we aim at establishing a more accurate relation between BLAs and the WHIM. Tejos et al. (2016) performed a novel experiment, searching for BLA features potentially produced by the WHIM at the redshifts where large-scale filaments should exist. They targeted a single QSO at $z \sim 0.79$ (SDSS J141038.39+230447.1; hereafter referred to as Q1410) whose unique sightline passes throughout seven independent cluster pairs at $0.1 < z < 0.5$, with impact parameters <3 Mpc to the inter-cluster axes connecting them. Theoretical models predict a high probability of finding a filamentary structure between close ($\lesssim$20 Mpc) and massive ($\gtrsim 10^{14} M_\odot$) galaxy cluster pairs (e.g. Colberg, Krughoff & Connolly 2005; González & Padilla 2010; Aragón-Calvo, van de Weygaert & Jones 2010). The authors identified seven BLAs with Doppler parameters >50 km s^{-1} in the spectrum of Q1410 at similar redshifts for six out of the seven cluster pairs and found a tentative excess of BLAs of a factor of ∼4 with respect to the field. These BLAs now became potential WHIM signatures and are the subject of further investigation presented in this paper.

We aim at determining the origin of these BLAs, in particular to assess whether these absorption features are produced by the IGM or by the haloes of intervening galaxies (e.g. Williams, Mulchaey & Kollmeier 2013). To discern between these cases, we used the physical impact parameter of nearby galaxies to the Q1410 sightline and the relative velocity offset between these galaxies and the BLAs. To this end, we have conducted a blind galaxy survey using the VLT/MUSE IFU (Bacon et al. 2014), with particular emphasis on the presence or lack of galaxies at the redshifts of the reported BLAs. Our survey used 1 hour of VLT/MUSE integration time, reaching redshift completeness level of ∼75 per cent down to magnitude $r_{\rm AB} = 25$ mag.

Our paper is structured as follows. In Section 2 we present and describe our data. In Section 3 we describe our survey, including the identification, characterization, completeness, and limitations. Section 4 presents our main results and in Section 5 we discuss them. A summary of our results and conclusions are presented in Section 6. For our analysis, we assume a Λcold dark matter cosmology based on the results of the Planck Collaboration XIII (2016).

2 DATA

2.1 VLT/MUSE integral field spectroscopy

We obtained VLT/MUSE data of an $\sim 1 \times 1$ arcmin^2 field containing Q1410 as part of the ESO programme 094.A-0575 (PI Tejos). The observations were taken with a seeing of ∼0.8 arcsec, sampled at 0.2×0.2 arcsec^2, with a spectral range from 4750 to 9350 Å, and a resolving power $R \sim 1770$–3590. A total of four exposures of 15 min each were used: two of them centred on the Q1410 field with a position angle PA = 0° and the remaining two centred on the brightest nearby galaxy at RA = $14^{\rm h}10^{\rm m}39\overset{\rm s}{.}8$ and Dec. = $+23^{\rm d}05^{\rm m}00\overset{\rm s}{.}8$ (J2000; ΔRA ≈ 19.4 arcsec; ΔDec. ≈ 14.2 arcsec) with a PA = 90°. As a result of this double pointing we obtained higher signal-to-noise ratio data where the two fields overlap for a full 1 h exposure. In the edges, the effective exposure time is 30 min.

Table 1. Summary of our observations described in Section 2.

VLT/MUSE observations			
Pointings		Exposure time	PA
RA	Dec.	(s)	(deg)
14:10:38.39	+23:04:47.18	2 × 900	0
14:10:39.79	+23:05:00.80	2 × 900	90

Table 1 summarizes these observations and Fig. 1 shows the targeted MUSE field (grey contours).

Data cubes have been reduced and combined using the standard MUSE pipeline version muse-1.4 (see http://www.eso.org/observing/dfo/quality/PHOENIX/MUSE/processing.html for details). As a post-processing reduction, we used the ZAP software (Soto et al. 2016) to perform a second-order sky subtraction, which uses principal components analysis (PCA) to isolate and remove residual sky subtraction features.

2.2 VLT/VIMOS imaging

Additional VLT/VIMOS data are available for this field. In particular, 2 min *R*-band pre-imaging was obtained as part of ESO programme 094.A-0575 (PI Tejos) for the mask preparation of multi-object spectroscopy (MOS) on the field. Unfortunately, the MOS data were never obtained. However, we are able to use the pre-imaging data as an astrometry reference frame for our MUSE data (see Fig. 1).

3 GALAXY SURVEY

3.1 Source identification

To identify the sources in the field and determine the aperture that best defines the spaxels[1] within each source we used SEXTRACTOR (Bertin & Arnouts 1996) in the 'white image'. This image corresponds to the sum of the flux at all wavelengths for each spaxel.

After performing a visual inspection to remove artefacts, we manually added 10 sources that were not detected by SEXTRACTOR but were still visible (but faint) in the 'white image'.

Finally, we used MUSELET (for MUSE Line Emission Tracker), a SEXTRACTOR-based PYTHON tool to detect emission lines in a data cube included in the MPDAF PYTHON package (Bacon et al. 2016), to search for additional emission-lines-only galaxies that were not visible in the 'white image' but show at least one strong emission line, and we added one source.

We ended up with a sample of 77 sources in the MUSE FoV, including the central QSO. For each source we extracted a 1D spectrum combining the spaxels inside the source aperture. The flux on each spaxel was weighted by a 'bright profile', proportional to the total flux of that spaxel in the white image. For the sources that were not originally detected by SEXTRACTOR, the aperture was arbitrarily defined as a circle containing most of the apparent flux. We estimated the $r_{\rm AB}$ magnitude for all the sources by convolving the data cube fluxes with a SDSS *r* transmission curve. This effectively creates a MUSE *r*-image. The zero-point of this image was calibrated by doing a linear fit with slope of unity between the SDSS modelled magnitudes and the SEXTRACTOR MAG AUTO magnitudes[2] of several cross-matched sources in the field (the photometry was only computed for the sources detected by SEXTRACTOR.). Our identified sources are summarized in Table 2.

3.2 Source characterization

Redshifts of each source were measured using REDMONSTER (Hutchinson et al. 2016). The code performs a χ^2 minimization between the observed spectrum and a set of theoretical models for galaxies, stars, and QSOs. These templates are modulated by a low-order polynomial mimicking the effects of galactic extinction, sky-subtraction residual, and possible spectrophotometric errors. We adopted a reliability scheme for the redshift measurements as follows:

(i) 'a' sources: these are the best characterized, showing at least two well-characterized features in their spectra.
(ii) 'b' sources: these are relatively well characterized, showing at least one well-identified feature and a possible second feature (marginal) in their spectra.
(iii) 'c' sources: these are uncertain, showing only one feature in their spectra (typically a single emission line). We included 'c' sources in our analysis in order to be conservative for ruling out the presence of galaxies near BLA features.
(iv) 'd' sources: these could not be characterized as they did not show any spectral feature. Most of them are fainter than $r_{\rm AB} = 24$ mag, and were excluded from our analysis.

Out of the 77 sources, we successfully obtained the redshifts for 52 of them (see Table 2). These include 42 obtained with REDMONSTER and 10 from visual inspection of strong emission lines. In Appendix D we present the REDMONSTER fits for the galaxies with a reliability level of 'a', 'b', and 'c'. For the galaxies showing only one strong emission line, we assume it to be Hα, or [O II] if the emission line shows a double peak profile. In these cases, the redshift was determined by fitting a Gaussian profile to the emission feature (a double Gaussian profile with a fixed separation was used for the [O II] doublet.) and we report only the redshift solution (without the uncertainties). The remaining 25 that could not be identified are listed in Table A1 in Appendix A.

We empirically estimated the uncertainties for the redshifts obtained with REDMONSTER (Hutchinson et al. 2016) by comparing the redshifts obtained for the same source in each individual exposure (see Section 2). We used a sub-sample of 25 sources for which REDMONSTER converged to a fit in at least two individual exposures (out of a total of 42 sources characterized with redshifts in the combined data cube), and studied the distribution of the differences between the redshifts obtained for each individual source. The dispersion in this distribution is due to the uncertainties of the redshift measurement in both exposures, and we determined its standard deviation to be $\sigma_{\rm diff} \approx 0.0002$. Therefore, assuming that both exposures have the same uncertainty, we can estimate an individual $\sigma_z \approx \frac{\sigma_{\rm diff}}{\sqrt{2}} \approx 0.00014$ for the REDMONSTER redshift measurements. Additionally, we looked for a cross-match between the SDSS spectroscopic catalogue and our survey. We found one single source (the central QSO) to match, and the redshift difference was consistent with our estimated σ_z.

We classified sources with redshifts based on their spectral types as follows:

[1] We refer to spaxel as a spatial sampling element that corresponds to a one-pixel spectrum in the data cube.

[2] We expect that the flux lost by the aperture defined by SEXTRACTOR accounts for less than 0.1 mag.

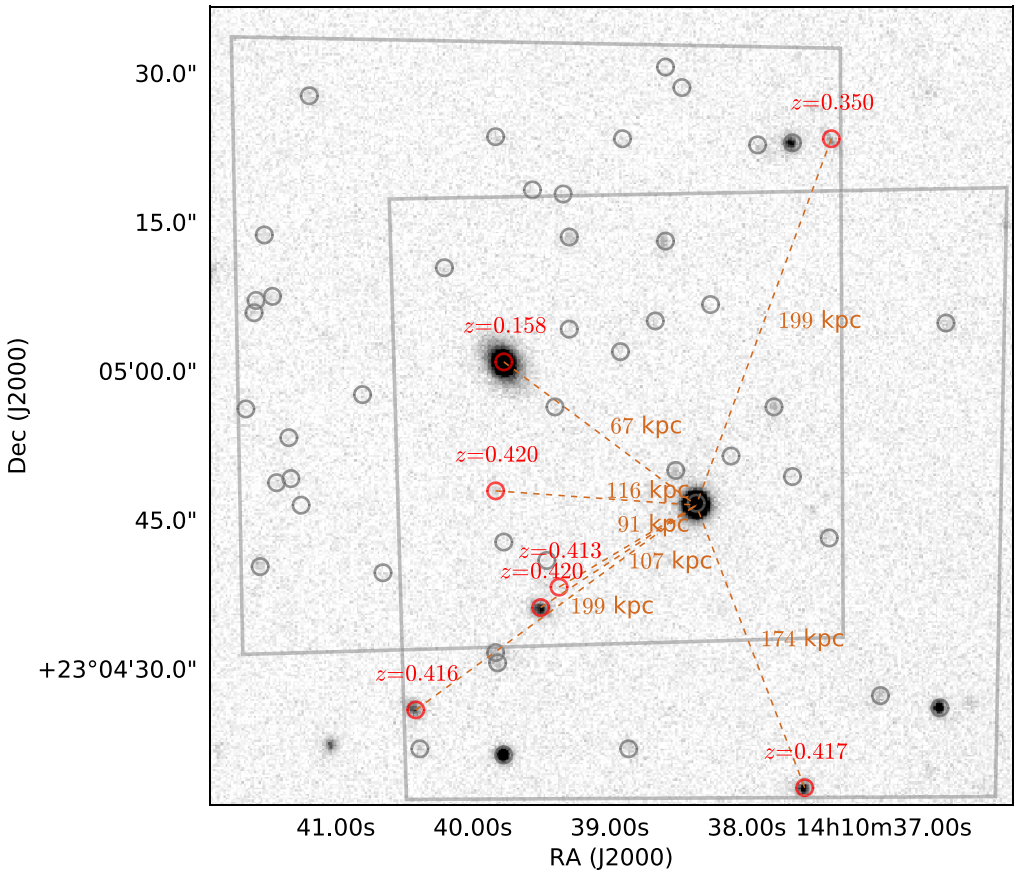

Figure 1. VLT/VIMOS image of our full MUSE field of view. The VLT/MUSE exposures are centred on the bright galaxy (upper left of the centre) and the QSO Q1410 (lower right of the centre), respectively (see Table 1). The grey contours mark the field of view of each individual VLT/MUSE exposure. We have characterized and measured redshifts for most sources brighter than $r = 25$ mag (see Table 2). Red circles show galaxies at redshifts within $\Delta v = \pm 1000\,\mathrm{km\,s^{-1}}$ of any BLA. Grey circles mark the rest of the sources characterized with a redshift.

(i) Star-forming (*SF*): galaxies that show strong emission lines and a blue continuum. These 38 sources correspond to 73 per cent of the sample with measured redshifts.

(ii) Non-star-forming (*non-SF*): galaxies that show a strong red continuum and an absence of emission lines. These six sources correspond to ∼11 per cent of the sample with measured redshifts.

(iii) Red star-forming (*SF-red*): These galaxies show both a strong red continuum and emission lines consistent with recent star formation events. These sources are rare accounting for ∼6 per cent of the sample with measured redshifts.

(iv) QSO: we find a quasar-like spectrum for three sources, corresponding to ∼6 per cent of the sample.

(v) Star: stellar-like spectrum. We identified a single star in our field.

(vi) Lyα emitter candidate (LAE): one source showed a prominent single emission line, asymmetric and extended to the red, at a $\lambda \approx 5045$ Å. Given its observed wavelength, this cannot be explained as an Hα emission. Furthermore, its profile and strength are inconsistent with this line being [O II]. Thus, we deem this source as a Lyα emitter candidate at $z \sim 3.15$.

The distribution of sources in the field is shown in Fig. 1. For each source with a redshift we estimated the proper transverse distance to the QSO sightline using our adopted Planck 2016 cosmology. We also calculated their absolute r_{AB} magnitude as follows:

$$M_{\mathrm{r}} = r_{\mathrm{AB}} - 5(\log(d_{\mathrm{L}}) - 1) - K_{\mathrm{corr}}, \quad (1)$$

where d_{L} is the luminosity distance in parsec. and K_{corr} is the corresponding K-correction for each galaxy (see Appendix B).

3.3 Survey characterization

In order to characterize the completeness of our survey we have used the apparent r_{AB} magnitudes. The left panel of Fig. 2 shows a histogram of sources per apparent r_{AB} magnitude bin, separating the sample for which good redshifts were obtained from the full sample. Our survey peaks at $r_{\mathrm{AB}} \approx 25$ mag. The sudden decline in the number of sources to fainter magnitudes marks our completeness limit. An apparent magnitude of $r_{\mathrm{AB}} = 25$ mag suggests a luminosity limit of $\sim 5 \times 10^8\,\mathrm{L}_{\odot}$ at $z \sim 0.45$. The central panel of Fig. 2 shows the fraction of sources that were successfully assigned a redshift as a function of r_{AB} bin. Our characterization reaches ∼75 per cent for $r_{\mathrm{AB}} \approx 25$ mag. The right panel shows the redshift distribution of our full sample coloured by spectral type.

Fig. 3 shows the distribution of impact parameter to the Q1410 sightline as a function of redshift. The hatched area in the upper left corner shows the limit of the FoV of VLT/MUSE as a function of redshift; regions in the hatched area are out of the effective VLT/MUSE coverage. At $z \approx 0.1$ our effective radial coverage is about 100 kpc, while at $z \approx 0.5$ we reach scales >300 kpc. The vertical black lines mark the redshift of the inter-cluster axes reported by Tejos et al. (2016) that show a BLA. The vertical dashed regions around these lines represent a rest-frame velocity window

Table 2. ($^{\perp}$): REDMONSTER did not converge to a z on these sources. Redshifts were calculated by a visual inspection on these cases. (*): Nearby Galaxies to the inter-cluster filaments. These sources are marked in red in Fig. 1. Sources were classified according to their spectral type. SF galaxies show strong emission lines and a blue continuum, non-SF galaxies show a strong red continuum and an absence of emission lines, and SF-red galaxies show a strong red continuum and emission lines. We also identified a Lyα emitter candidate, which is classified as LAE. Sources where r is undefined were not detected by SEXTRACTOR and we manually included them in this survey. The uncertainties of the REDMONSTER redshift measurements in Column 9 are of the order of $\sim$0.00014.

Sources characterized in our survey										
ID	Object	RA J2000	Dec. J2000	Impact parameter (arcsecs)	(kpc)	r_{AB}	M_r	z	Class	Reliability
(1)	(2)	(3)	(4)	(5)	(6)	(7)	(8)	(9)	(10)	(11)
1	J141038.37+230446.5	212.65987	23.07958	0.0	0	17.35	− 26.20	0.7961	QSO	a
2	J141038.52+230449.7	212.66050	23.08047	3.8	29	24.15	− 22.08	0.7976	SF-red	a
3	J141038.11+230451.3	212.65879	23.08092	6.0	46	25.21	− 19.31	0.7966	SF	c
4	J141037.66+230449.2	212.65692	23.08033	10.2	79	24.39	− 18.75	0.8315	SF	a
5	J141037.80+230456.2	212.65750	23.08228	12.5	70	23.55	− 19.20	0.4048	SF	b
6	J141037.40+230443.0	212.65583	23.07861	13.8	107	24.48	− 19.91	0.7940	SF	b
7	J141039.46+230440.7	212.66442	23.07797	16.1	112	23.35	− 19.55	0.6171	SF	a
8*	J141039.37+230438.1	212.66404	23.07725	16.2	91	24.77	− 17.16	0.4126	SF	c
9	J141038.92+230501.8	212.66217	23.08383	17.1	137	24.82	− 21.22	0.9093	SF	b
10	J141039.40+230456.2	212.66417	23.08228	17.2	149	24.94	− 20.02	1.4865	SF	b$^{\perp}$
11	J141038.67+230504.8	212.66112	23.08467	18.8	136	24.37	− 19.41	0.6750	SF	a
12*	J141039.50+230435.9	212.66458	23.07664	18.9	107	21.32	− 21.29	0.4199	SF-red	a
13	J141039.77+230442.5	212.66571	23.07847	19.7	171	24.29	− 19.55	1.4596	SF	b$^{\perp}$
14	J141038.27+230506.4	212.65946	23.08511	19.9	144	–	–	0.6676	SF	c
15*	J141039.84+230447.8	212.66600	23.07994	20.3	116	23.71	− 18.83	0.4198	SF	a
16	J141039.29+230504.1	212.66371	23.08447	21.7	169	24.31	− 146.55	3.1500	LAE	c$^{\perp}$
17*	J141039.77+230500.7	212.66571	23.08353	24.0	67	18.93	− 20.94	0.1577	Non-SF	a
18	J141039.83+230431.4	212.66596	23.07539	25.2	195	22.10	− 22.41	0.8125	SF	a
19	J141038.86+230421.8	212.66192	23.07272	25.6	197	23.24	− 21.14	0.7963	SF	b
20	J141039.82+230430.4	212.66592	23.07511	25.7	219	23.12	− 20.73	1.2070	SF	b$^{\perp}$
21	J141038.60+230512.8	212.66083	23.08689	26.5	171	22.78	− 20.43	0.5246	SF	a
22	J141037.02+230427.0	212.65425	23.07417	27.0	176	22.90	− 19.99	0.5348	SF	a
23	J141039.29+230513.3	212.66371	23.08703	29.7	114	23.07	− 17.71	0.2354	SF	a
24*	J141037.58+230417.9	212.65658	23.07164	30.6	174	21.96	− 21.12	0.4169	Non-SF	a
25	J141036.54+230504.7	212.65225	23.08464	31.1	269	23.92	− 22.54	1.3583	SF	b$^{\perp}$
26	J141039.78+230421.1	212.66575	23.07253	32.0	256	20.44	− 23.43	0.8975	QSO	b
27	J141036.59+230425.9	212.65246	23.07386	32.1	277	21.13	− 23.82	1.3400	QSO	b
28	J141040.65+230439.5	212.66937	23.07764	32.2	278	25.69	− 17.36	1.3118	SF	b$^{\perp}$
29	J141039.34+230517.6	212.66392	23.08822	33.9	289	23.69	− 21.48	1.2081	SF	c$^{\perp}$
30	J141040.20+230510.2	212.66750	23.08617	34.6	300	24.32	− 21.34	1.4305	SF	b$^{\perp}$
31*	J141040.42+230425.6	212.66842	23.07378	35.2	199	21.51	− 21.26	0.4159	Non-SF	a
32	J141040.81+230457.3	212.67004	23.08258	35.4	289	99.00	53.56	0.9722	SF	b
33	J141039.56+230518.1	212.66483	23.08836	35.6	308	24.44	− 22.46	1.3849	SF	b$^{\perp}$
34	J141037.92+230522.5	212.65800	23.08958	36.5	238	22.41	− 20.53	0.5347	SF	a
35	J141040.38+230421.7	212.66825	23.07269	37.2	–	23.40	–	0.0000	Star	a
36	J141038.91+230523.1	212.66212	23.08975	37.4	318	24.71	− 21.80	1.1972	SF	b
37	J141037.67+230522.8	212.65696	23.08967	37.6	238	21.44	− 22.41	0.5079	Non-SF	a
38*	J141037.38+230523.1	212.65575	23.08975	39.1	199	22.39	− 19.69	0.3502	SF	a
39	J141041.26+230446.3	212.67192	23.07953	39.9	307	24.94	− 27.97	0.7898	Non-SF	c
40	J141041.33+230448.9	212.67221	23.08025	40.9	327	24.78	− 21.48	0.8960	SF	a
41	J141041.34+230453.0	212.67225	23.08139	41.5	332	24.39	− 27.77	0.8964	SF	b
42	J141038.48+230528.4	212.66033	23.09122	41.9	325	24.95	− 21.32	0.8123	SF	c
43	J141039.83+230523.3	212.66596	23.08981	42.0	297	23.00	− 20.95	0.6369	SF	a
44	J141041.44+230448.6	212.67267	23.08017	42.4	340	25.09	− 31.85	0.8979	SF-red	a
45	J141038.59+230530.5	212.66079	23.09181	44.1	97	24.47	− 14.58	0.1180	SF	c
46	J141041.55+230440.1	212.67312	23.07781	44.3	339	23.35	− 22.45	0.7741	SF	a
47	J141041.66+230455.9	212.67358	23.08219	46.4	370	24.52	− 31.97	0.8889	SF	b
48	J141041.47+230507.3	212.67279	23.08536	47.6	406	24.01	− 22.36	1.2077	SF	b$^{\perp}$
49	J141041.59+230505.7	212.67329	23.08492	48.4	358	23.84	− 21.85	0.7086	SF	a
50	J141041.58+230506.9	212.67325	23.08525	48.8	408	24.90	− 24.02	1.0799	SF	b
51	J141041.52+230513.5	212.67300	23.08708	51.2	428	24.71	− 39.93	1.0793	Non-SF	a
52	J141041.19+230527.5	212.67162	23.09097	56.5	481	23.13	− 22.36	1.1980	SF	c

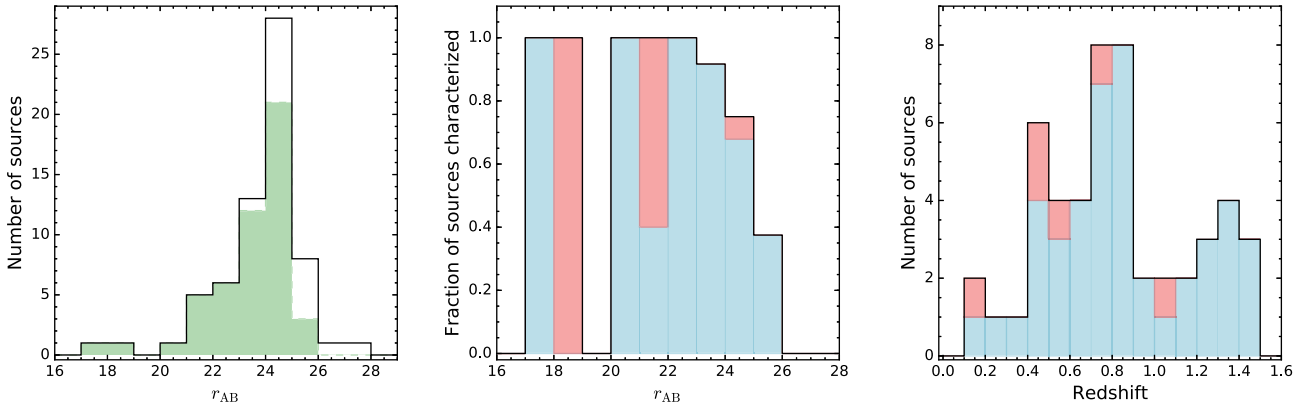

Figure 2. Left: survey histogram coloured in green for our sample with measured redshifts. The black line shows the distribution for the whole sample detected by SEXTRACTOR. Our detection threshold is at $r \sim 25$ mag. Centre: the completeness fraction of the redshift survey. The star-forming galaxies are shown in blue and the non-star-forming galaxies in red. The black contour marks our full sample. We reach to ∼75 per cent successful characterization fraction at an apparent magnitude $r_{AB} = 25$ mag. Right: the redshift distribution of our full characterized sample coloured by star-forming and non-star-forming fraction same as the central panel. The LAE candidate at $z \approx 3.15$ is not shown here.

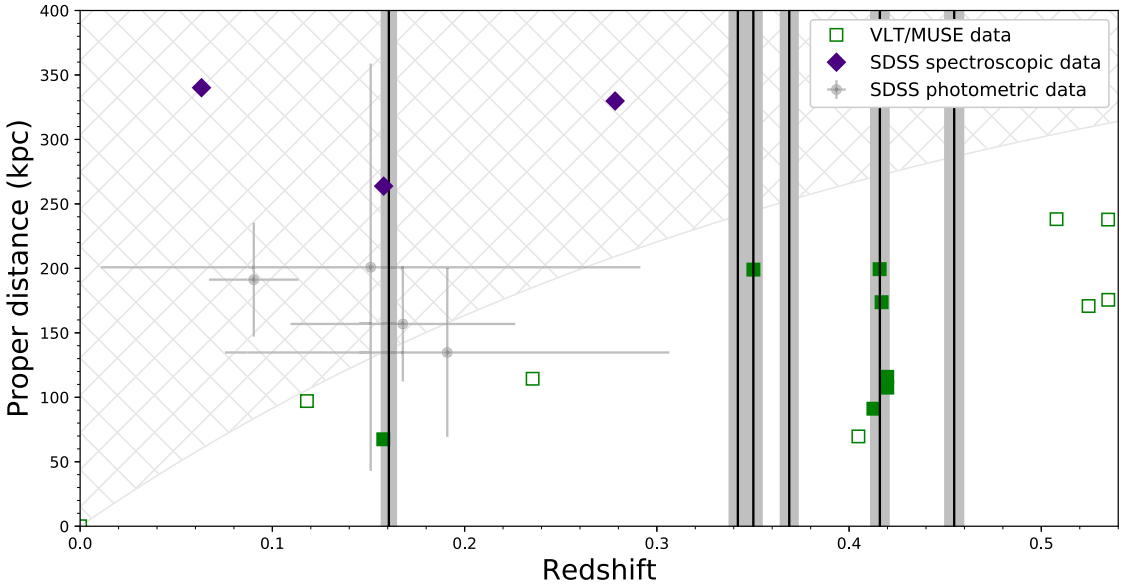

Figure 3. Distribution of impact parameter to the Q1410 sightline as a function of redshift. Our VLT/MUSE sample of galaxies is shown in green squares. SDSS galaxies are shown in violet diamonds and grey circles (see Section 3.4 for details). We only show here galaxies in the SDSS photometric catalogue that are outside the MUSE FoV. The vertical black lines surrounded by a shaded region mark the redshift of the inter-cluster axes $\pm 1000\,\mathrm{km\,s^{-1}}$ from its rest frame. Filled squares mark sources in the VLT/MUSE sample that are located within $\pm 1000\,\mathrm{km\,s^{-1}}$ of an inter-cluster axis and will be the subject of further analysis. The hatched area in the upper left corner is outside the MUSE FoV and shows the approximate edges of our spectroscopic survey

of $\Delta v = \pm 1000\,\mathrm{km\,s^{-1}}$ around these redshifts. Excluding galaxies at the redshifts of the cluster-pairs, we found nine sources brighter than apparent magnitude $r_{AB} = 23$ mag. This represents a density of $22\,500 \pm 7\,500\,\mathrm{deg^{-2}}$, assuming a Poissonian error, which is consistent with the density of $\sim 20\,000\,\mathrm{deg^{-2}}$ found by the VVDS survey (Le Fèvre et al. 2005).

Table 2 summarizes the characterization of the sources in our full survey.

3.4 SDSS galaxies

As mentioned before, at low-z our VLT/MUSE survey has a relatively limited FoV. In particular, at $z \approx 0.16$ we would need to triplicate our current FoV to cover a physical impact parameter of ∼300 kpc, which has been suggested for the so-called circum-galactic medium (CGM; Prochaska et al. 2011; Borthakur et al. 2016). In order to partially compensate this limitation, we have included galaxies with spectroscopic redshifts from the SDSS (SDSS Collaboration et al. 2016). These galaxies are marked with diamonds in Fig. 3. At $z \approx 0.16$ we found three SDSS galaxies, the closest being at an impact parameter of ∼260 kpc to the QSO sightline. The remaining two are located at an impact parameter of >450 kpc and are not shown in Fig. 3 (see Table C1).

We have also looked for evidence of galaxies that we could be missing outside the MUSE FoV at the redshifts of the inter-cluster axis in the SDSS photometric catalogue. We found ∼400 additional galaxies closer than 4 arcmin around the line of sight, corresponding to a transverse distance of ∼500 kpc at $z = 0.1$. Given the high uncertainties in the photometric redshifts (and consequently, in the estimated physical impact parameters), we have looked only

for galaxies whose physical impact parameters may lie within two times their inferred virial radii to the QSO sightline, given their inferred stellar masses. Stellar masses were obtained from their photometry using the relation presented in Taylor et al. (2011). We then estimated their virial masses and virial radii in the same fashion as explained in Section 4.1. To be conservative, we considered the lower value of the error bar for the physical impact parameter and the upper value of the error bar for the virial radius (this uncertainty comes from the dispersion of ∼0.1 dex in the stellar mass relation of Taylor et al. (2011).). We found eight sources satisfying this condition between its impact parameter and virial radii at photometric redshifts $z < 0.5$, of which four are outside the MUSE FoV and are shown in Fig. 3 as grey circles (the other four were already detected by our MUSE spectroscopic survey.). We found that two of these have photometric redshifts $z \lesssim 0.2$ with relatively low redshift uncertainties, making them unlikely to be associated with any of our BLAs at $z > 0.3$. However, the remaining two need further analysis. Given that the uncertainties in the inferred proper impact parameter comes from the large uncertainty in the photometric redshift estimation, we can check if these galaxies could be related to the BLA at $z = 0.3422$ (or higher), by comparing their virial radius with the impact parameter that would have at that redshift. If we set these galaxies to be at that redshift, we obtain that their impact parameter would be higher than four times their estimated virial radius; if one of those galaxies is at $z \approx 0.3422$ (or higher), it would be at a large enough impact parameter for it not to be physically associated with the BLA. Thus, we conclude that we are likely not missing any galaxy outside the FoV of MUSE that could be directly associated with a BLA at redshift $z = 0.3422$ (or higher).

4 RESULTS

4.1 Galaxies at BLA redshifts

We now focus on galaxies that may be related to the BLAs of interest, i.e. those observed at redshifts of cluster-pairs as reported by Tejos et al. (2016). From our blind galaxy survey, we selected the subsample of galaxies lying within $\Delta v \pm 1000\,\mathrm{km\ s^{-1}}$ from any of the aforementioned BLAs. We found seven out of the 52 characterized sources of the sample satisfying this criterion (filled green squares in Fig. 3), for which stellar masses, halo masses, virial radii, and virial velocity dispersions were estimated. Stellar masses were calculated using the STARLIGHT software (Cid Fernandes et al. 2005), which performs a spectral synthesis analysis assuming a Chabrier (2003) initial mass function (IMF). Since StarLight does not provide an estimation of the uncertainty for the inferred stellar masses, we assume its error to be 0.25 dex based on the analysis presented in Li et al. (2017, see their fig. 1). Halo masses were estimated from the stellar masses by assuming the bijective relation between the two as given by Moster et al. (2010). We consider this inferred halo mass as a virial mass, $M_{\rm vir}$ of a galactic system and estimated a virial radius as,

$$R_{200} = \left(\frac{M_{\rm vir}}{\frac{4}{3}\pi 200 \rho_{\rm c}(z)} \right)^{1/3}, \qquad (2)$$

i.e. R_{200} is the radius of the spherical volume where $M_{\rm vir}$ is contained at 200 times the critical density of the Universe at a given redshift, $\rho_{\rm c}(z)$. Velocity dispersions for each galaxy were estimated as:

$$\sigma_{\rm vir} = \sqrt{\frac{G M_{\rm vir}}{R_{200}}}. \qquad (3)$$

Table 3. Galactic parameters of galaxies found to be close to the inter-cluster filaments. The Δv of each Galaxy with respect to the nearby BLAs is shown in Fig. 5, where each galaxy is labelled according to their ID in this table. Column 5 corresponds to the physical impact parameter of each galaxy to the Q1410 sightline in kpc. Column 7 marks the Δv of the galaxy with respect to the closest BLA in Fig. 5.

Galaxies nearby known BLAs						
ID	z	$M_{\rm vir}$ $10^{11}\mathrm{M}_\odot$	$R_{\rm vir}$ kpc	I.P. kpc	$\sigma_{\rm vir}$ km s^{-1}	Δv km s^{-1}
(1)	(2)	(3)	(4)	(5)	(6)	(7)
1	0.1577	8.0±3.9	186±30	67	136 ± 35	745
2	0.3502	3.0±1.0	125±14	199	102 ± 18	−7
3	0.4126	0.8±0.2	77±7	91	65 ± 10	−174
4	0.4159	3.4±1.2	126±14	199	107 ± 20	−863
5	0.4169	7.2±3.3	162±24	173	138 ± 33	700
6	0.4198	3.1±1.1	122±13	115	104 ± 19	80
7	0.4199	2.6±0.9	115±12	107	98 ± 17	78

Uncertainties in $M_{\rm vir}$, R_{200}, and $\sigma_{\rm vir}$ were estimated by propagating the adopted error in the stellar masses. Table 3 summarizes these inferred properties for our sample galaxies near BLAs.

In the following, we use the scales given by R_{200} and $\sigma_{\rm vir}$ of each galaxy to discriminate whether it could be directly associated with a BLA feature or not.

4.2 Potential association of galaxies to known BLAs

In Tejos et al. (2016) the authors identified seven BLA features at six different redshifts, related to six out of the seven inter-cluster axes at $0.1 < z < 0.5$. As seen in Fig. 3, three out of the six relevant inter-cluster axes show at least one nearby galaxy.[3]

In order to discriminate whether a BLA may be associated with one (or more) of these galaxies, we consider both their impact parameters and their rest-frame absolute velocity difference $|\Delta v|$. We define $\eta = \frac{R_{\rm projected}}{R_{\rm vir}} \frac{|\Delta v|}{\sigma_{\rm vir}}$ (sometimes called caustic lines) to quantify the global environment. In Fig. 4, we show the impact parameter of each galaxy versus $|\Delta v|$ with respect to each BLA found at that redshift, in units of $R_{\rm vir}$ and $\sigma_{\rm vir}$ of the corresponding galaxy. Each galaxy–BLA pair is represented by a square coloured by the redshift of the galaxy given by the colour bar. In principle, if a BLA is close to a galaxy both in projection and velocity at values comparable to the $R_{\rm vir}$ and $\sigma_{\rm vir}$, respectively, it would indicate that the BLA may have been produced by the galaxy halo rather than by the WHIM. $\eta < 2$ should mark the limit for a gravitationally bounded system (Shen et al. 2017, and references therein).[4] For completeness, in Fig. 5 we show a portion of the Q1410 spectrum for each one of the inter-cluster axes that present a BLA on its rest frame. Nearby galaxies are marked with arrows labelled with the IDs given in Table 3.

In the following, we give a brief description of each BLA system:

(i) The two BLAs at $z \approx 0.4160$ seem to be located in a galaxy group environment (with at least five galaxies). There are two galaxies at an impact parameter $\rho/R_{\rm vir} \sim 0.95$ and $|\Delta v|/\sigma_{\rm vir} \sim 0.7$, both below the $\eta = 1$ curve. Thus, we cannot rule out that these BLAs

[3] Note that there are two BLAs at $z \approx 0.416$, for which there is also a group of galaxies (see Table 4).

[4] This limit was determined in the context of galaxy cluster physics, but we assume the same limit since the involved mechanisms are the same.

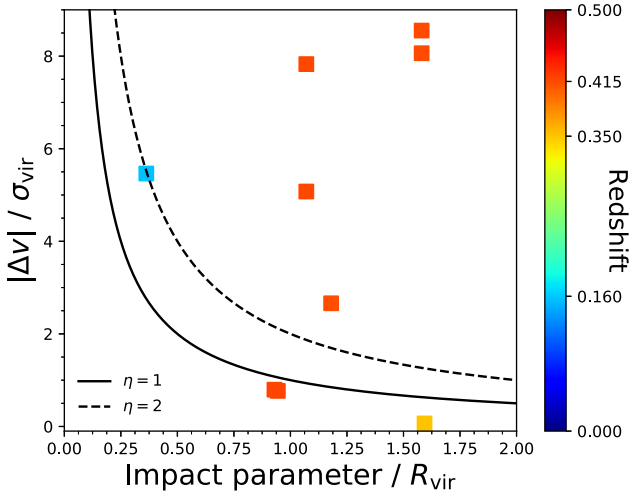

Figure 4. Each square represents a single galaxy–BLA combination identified from our sample, representing a total of seven galaxies and four absorbers across three separate intra-cluster axes. The panel shows the relationship between potential host galaxies and absorbers in terms of a velocity difference and impact parameter to the QSO sightline in units of σ_{vir} and R_{vir}, respectively. The η is defined as $\frac{R_{projected}}{R_{vir}} \frac{|\Delta v|}{\sigma_{vir}}$ and is used to quantify the global environment. $\eta < 2$ should mark the limit for a gravitationally bounded system (Shen et al. 2017).

may have been produced in the galaxy group halo (as opposed to WHIM).

(ii) The BLA at $z \approx 0.3502$ is very close to a strong narrow H I system that shows metal-enriched gas (Tejos et al. 2016). It also has $|\Delta v|/\sigma_{vir} < 0.5$ to the closest galaxy observed and it is located below the $\eta = 1$ curve. This places the absorption close to a galactic halo and its origin is uncertain. Moreover, our revised analysis of the absorption features in Q1410 (see Appendix E) deems this BLA as highly uncertain.

(iii) The BLA at $z \approx 0.1606$ has $\rho/R_{vir} \sim 0.4$ but $|\Delta v|/\sigma_{vir} \sim 5.4$. This places this BLA near the limit of $\eta = 2$. However, this latter BLA also shows a nearby galaxy from SDSS at an impact parameter of $\approx$260 kpc to the sightline of the QSO with $|\Delta v| \approx 800\,\mathrm{km\ s^{-1}}$. Moreover, SDSS shows two more galaxies at higher impact parameters ($\sim$450 kpc), both at $|\Delta v| \sim 560\,\mathrm{km\ s^{-1}}$ (See Section 3.4).

(iv) The BLAs at $z \approx 0.3422$, $z \approx 0.3689$, and $z \approx 0.4547$ do not show any potential host galaxy to a luminosity limit of $L \approx 4 \times 10^8\,L_\odot$, corresponding to $\approx 0.01\,L_*$ (Zucca et al. 2006; McNaught-Roberts et al. 2014) (or $\sim 3 \times 10^8 L_\odot$ for $z \approx 0.3422$ and $\sim 5 \times 10^8 L_\odot$ for $z \approx 0.4547$). We note that at those redshifts, our FoV covers impact parameters of $\approx$ 270, 280, and 320 kpc[5], respectively, comparable to the virial radius of an L_* galaxy. Still, as explained in Section 3.4, we have searched for photometric galaxies outside the MUSE FoV from the SDSS data, and found that the presence of such luminous galaxies right outside the FoV is unlikely.

As mentioned above, a detection limit of $r_{AB} = 25$ mag implies a luminosity limit of $\sim 2 - 5 \times 10^8 L_\odot$ at $z \approx 0.1 - 0.45$. We detected seven galaxies brighter than this luminosity limit at the redshifts of the inter-cluster axes. We used a Schechter luminosity function to estimate the number of fainter galaxies that we could be missing given that we detected seven galaxies brighter than the luminosity limit. We used $\alpha = -1.25$ and $L_* = 3.15 \times 10^{10} L_\odot$ (McNaught-Roberts et al. 2014) as the parameters for the luminosity function and $L_{min} = 1 \times 10^6 L_\odot$ (Sawala et al. 2016) as a conservative luminosity lower limit to integrate the luminosity function (although the existence of even fainter galaxies is possible such as fossils galaxies). From this, we estimate that <1 faint galaxies may be missing. Thus, it is unlikely our analysis is significantly affected by an undetected population of faint galaxies.

Regarding large-scale structure, we remind the reader that we found evidence of a galaxy group in only one out of the seven inter-cluster axes probed by our MUSE survey (at $z \approx 0.461$). The lack of galaxy overdensities in the other six does not rule out the existence of a filamentary structure in them. According to the halo mass function presented in Reed et al. (2007), the average density of dark matter haloes more massive than $10^{12}\,h^{-1}M_\odot$ is $0.004\,(h^{-1}\mathrm{Mpc})^3$. The volume sampled by MUSE inside a single filament is about 400 kpc × 400 kpc × 6 Mpc. Considering an overdensity of a factor of ≈3 in the filaments with respect to the mean density of the Universe, and the fact that the sightline passes through seven independent inter-cluster axes, we would expect to detect ≈0.02 dark matter haloes more massive than $10^{12} M_\odot$ associated with the filaments in the MUSE FoV. This is consistent with the single structure found in our data, within the Poissonian error.

4.3 Revision to the BLAs reported by Tejos et al. (2016)

Given the intrinsic difficulty for finding and characterizing broad and shallow absorption features in QSO spectra, it is expected that some of the reported BLAs may be subject to large systematic uncertainties. In Appendix E we have performed independent analyses for quantifying potential systematic effects. We concluded that, with the exception of the putative BLA at $z = 0.3502$ (that could be even a narrow H I), all the other BLAs in inter-cluster axes reported by BLA have systematic uncertainties well below or consistent with the reported statistical uncertainties. Thus, given that the absorption feature at $z = 0.3502$ has already been discarded from our 'clean' sample of BLAs on the basis of the existence of a potential galaxy counterpart (see Section 4.2), we expect that the rest of the BLA sample is not much affected by systematic effect in the analysis of Tejos et al. (2016). In the following, we will use their reported fit parameters for these BLAs as these agree well with our new analyses within statistical uncertainties. We note that according to Tejos et al. (2016), this sample of BLAs is complete down to a rest-frame equivalent width of $W_r = 0.039$ Å (see their fig. 5). There are two BLAs in our sample that are close to this limit: the one at $z = 0.3689$ (with $W_r = 0.089 \pm 0.023$ Å) and the one at $z = 0.4202$ (with $W_r = 0.090 \pm 0.024$ Å). The latter is already discarded from our 'clean' sample because of the presence of a group of galaxies at a similar redshift, and we have opted to keep the former in.

In summary, our analyses indicate that three BLAs in inter-cluster axes do not show nearby potential host galaxy haloes to stringent luminosity limits and their fit parameters are robust to tests on potential systematic effects (including data reduction, continuum estimation, and Voigt profile fitting software). We consider these three BLAs to be good WHIM candidates. In the following, we will use their properties to assess the baryon content implied by these BLAs assuming these are genuine WHIM signatures.

4.4 Density characterization of WHIM

For the three BLAs that do not show any nearby galaxy we can obtain the neutral hydrogen column density $N_{H\,I}$ and the Doppler parameter

[5] These numbers may vary since our FoV is not symmetrically distributed around Q1410.

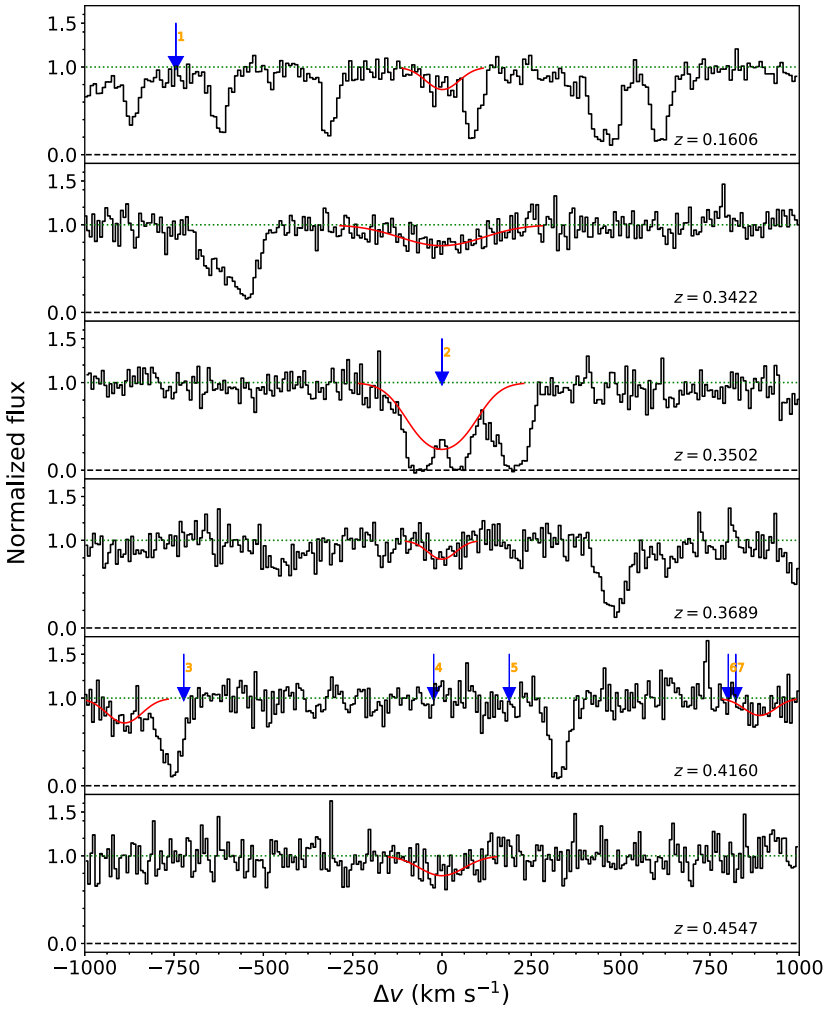

Figure 5. Panels show BLAs in the Q1410 COS spectrum within $\Delta v = \pm 1000\,\mathrm{km\,s^{-1}}$ from the z of the inter-cluster axes. The panels are ordered by z. Arrows with numbers represent the redshifts of nearby galaxies, which are numbered according to Table 3 (Column 1).

b directly from the observed spectrum (Tejos et al. 2016). We split the observed Doppler parameter into two different components, thermal ($b_{\rm th}$) and non-thermal ($b_{\rm non\text{-}th}$),

$$b_{\rm obs} = \sqrt{b_{\rm th}^2 + b_{\rm non\text{-}th}^2}. \quad (4)$$

The thermal broadening only depends on the temperature (T) of the gas,

$$b_{\rm th} = \sqrt{\frac{2k_{\rm b}T}{m}} \approx 0.129\sqrt{\frac{T}{A}}\,\mathrm{km\,s^{-1}} \quad (5)$$

where $k_{\rm b}$ is the Boltzmann constant, m is the gas particle mass, and A is the atomic weight of the element. For H I, equation (5) follows (e.g. Richter et al. 2006b):

$$T \approx 60\left(\frac{b_{\rm th}}{\mathrm{km\,s^{-1}}}\right)^2\,\mathrm{K}. \quad (6)$$

On the other hand, non-thermal broadening mechanisms include turbulence, Hubble flow, line blending, etc. In overdensities like inter-cluster filaments we may expect that turbulence dominates, and we parametrize it as being proportional to the thermal broadening, such that $b_{\rm non\text{-}th} \approx b_{\rm turb} \approx \alpha b_{\rm th}$. This would imply:

$$b_{\rm obs}^2 \approx b_{\rm th}^2 + b_{\rm turb}^2 \approx b_{\rm th}^2(1+\alpha^2). \quad (7)$$

Cosmological hydrodynamical simulations from the OWLS project suggest $0 \leq \alpha \leq 1.3$ with a dependence on H I column density (Tepper-García et al. 2012, see their fig. 5). If we restrict to absorption lines with column densities in the range of $10^{13} < N < 10^{14.5}\,\mathrm{cm^{-2}}$ these simulations suggest $\alpha \approx 0 - 0.8$. We also note that Richter, Fang & Bryan (2006a) found values of $\alpha \approx 0.5$ from an independent simulation. Observationally, one could estimate α by comparing the observed Doppler parameters in systems with both H I and O VI, assuming they both come from the same gas in thermal equilibrium (Rauch, Haehnelt & Steinmetz 1997). Savage et al. (2014) and Stocke et al. (2014) presented a sample with aligned[6] H I and O VI absorbers. Using the different line widths of both components, and given that the thermal Doppler broadening depends on the temperature and on the atomic mass (see equation 5), they estimated the $b_{\rm non\text{-}th}$ contribution for each system. Considering only those systems where $b(\mathrm{H\,I})_{\rm obs} > 40\,\mathrm{km\,s^{-1}}$ (18 out of their total sample) we studied the distribution for the α parameter in their sample. Their α values are distributed between $0.2 < \alpha < 2.1$, with an average of $\approx$0.7 where most of the values (15/18) have $\alpha < 1$.

[6] $\Delta v < 10\,\mathrm{km\,s^{-1}}$ between the H I and O VI components.

Given that the BLAs in our sample do not show O VI, we cannot empirically determinate the non-thermal broadening for our BLAs individually in this manner. Based on these theoretical and empirical studies, in the following we assume a fiducial value of $\alpha = 0.7$, but will leave its dependency explicit in the calculations. From equation (7) we then obtain the value of $b_{\rm th}$ given $b_{\rm obs}$. Then we can estimate the temperature of the gas using equation (6). In order to calculate the total gas column density, it is necessary to know the ionization fraction of the gas,

$$f_{\rm ion} \equiv \frac{N_{\rm H\,I} + N_{\rm H\,II}}{N_{\rm H\,I}} \approx \frac{N_{\rm H\,II}}{N_{\rm H\,I}}, \tag{8}$$

i.e. the number of ionized hydrogen per neutral ones. If we take into account a pure CIE scenario, $f_{\rm ion}$ depends only on the temperature of the gas and can be approximated by the polynomial (Sutherland & Dopita 1993):

$$\log(f_{\rm ion}) \approx -13.9 + 5.5\log\left(\frac{T}{\rm K}\right) - 0.33\log\left(\frac{T}{\rm K}\right)^2. \tag{9}$$

However, Richter et al. (2006a) found that at the typical WHIM densities, photoionization from the UV background also contributes; neglecting it may underestimate the baryon density up to 50 per cent. Their combined photoionization plus collisional ionization model suggests a linear relation between $\log(f_{\rm ion})$ and $\log(T)$ as

$$\log(f_{\rm ion}) \approx -0.75 + 1.25\log\left(\frac{T}{\rm K}\right) \tag{10}$$

for which $f_{\rm ion}$ as a function of $b_{\rm obs}$ and α can be written as:

$$f_{\rm ion} \approx 0.1778\left(\frac{T}{K}\right)^{1.25} \approx 29.7\left(\frac{b_{\rm obs}/{\rm km\,s^{-1}}}{\sqrt{1+\alpha^2}}\right)^{\frac{5}{2}}. \tag{11}$$

Here we use equation (11) to infer $f_{\rm ion}$ and then calculate the total gas column density $N_{\rm H} \approx N_{\rm HII}$ for each individual BLA simply as $N_{\rm H} \approx f_{\rm ion} N_{\rm H\,I}$.

We assume a radial volumetric density profile for the inter-cluster filaments parametrized by an exponent Γ of the form

$$n_{\rm H}(r) = n_0 \frac{1}{1+\left(\frac{r}{r_{1/2}}\right)^{\Gamma}}, \tag{12}$$

where r is the radial distance to the filament axis (i.e. in cylindrical coordinates), n_0 is the peak density at filament centre (except when $\Gamma = 0$), and $r_{1/2}$ is a characteristic radius such that $n_{\rm H}(r_{1/2}) = n_0/2$. Given this radial density profile we can solve

$$N_{\rm H} = \int n_{\rm H} {\rm d}l \tag{13}$$

to estimate a mean particle density $\overline{n_{\rm H}}$ inside the filaments given our inferred $N_{\rm H}$. In the following, we use simple models based on two different values of Γ.

4.4.1 *Uniform density model ($\Gamma = 0$)*

The simplest case is a model in which the filament is a cylindrical structure with uniform density profile, i.e. $\Gamma = 0$ in 12. In this case,

$$N_{\rm H} = \int_0^L \frac{n_0}{2}{\rm d}l \equiv \int_0^L \overline{n_{\rm H}}{\rm d}l = \overline{n_{\rm H}}L. \tag{14}$$

Thus $\overline{n_{\rm H}} = N_{\rm H}/L$ where L corresponds to the distance along the filament intersected by the QSO sightline. As a first estimation, we can use the average diameter of the cosmic-web filaments of ≈6 Mpc as found by simulations (e.g. González & Padilla 2010; Aragón-Calvo et al. 2010; Cautun et al. 2014). The true relation between L and the radius of the filament is uncertain, and it depends on the angle of incidence (θ) and the impact parameter relative to the radius of the filament ($\equiv \epsilon R$) of the sightline to the centre (e.g. see Fig. 6 for an schematic). If $\theta \neq 0$ and $\epsilon = 0$, i.e. the sightline is not perpendicular to the filament but it passes through its centre, $L = 2R/\cos(\theta)$. On the other hand, if $\theta = 0$ and $\epsilon \neq 0$, i.e. the sightline is perpendicular to the filament but has an impact parameter of ϵR, $L = 2\sqrt{1-\epsilon^2}R$ (see Fig. 6). Thus, the mean density value for each BLA can be estimated as

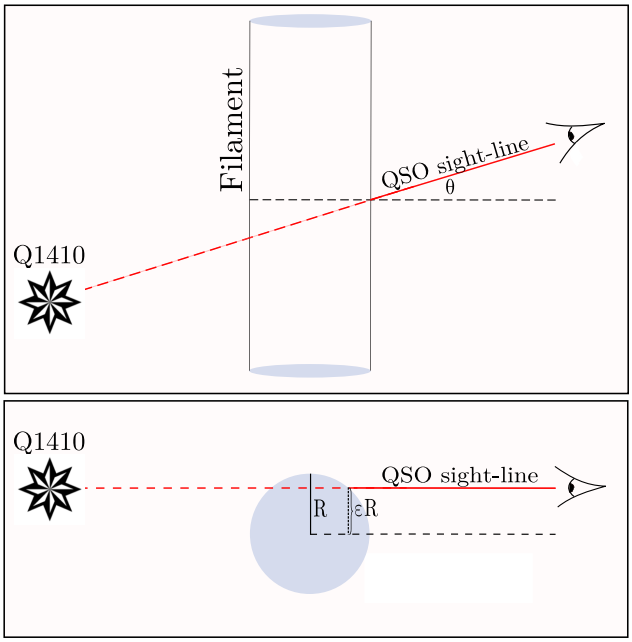

Figure 6. Schematic representation along the sightline (in red) of the geometry assumed for deriving WHIM density. A filamentary structure is represented by a cylinder. θ is the angle between the sightline and the perpendicular axis to the filament. The impact parameter of the sightline with respect to the centre is parametrized by the fraction ϵ.

$$\overline{n_{\rm H}} = \frac{N_{\rm H}}{L} = \frac{f_{\rm ion} N_{\rm H\,I}\cos(\theta)}{2\sqrt{1-\epsilon^2}R}. \tag{15}$$

For simplicity, we assume a fiducial case where the sightlines are all perpendicular and intersect the filaments at their centres. By averaging the $\overline{n_{\rm H}}$ for the three BLAs with no galaxies nearby we obtain

$$\langle\overline{n_{\rm H}}\rangle = 5.9\times10^{-6}\left(\frac{1-\epsilon^2}{1}\right)^{-\frac{1}{2}}\left(\frac{\cos(\theta)}{1}\right)\left(\frac{1+\alpha^2}{1.49}\right)^{-\frac{5}{4}}{\rm cm}^{-3} \tag{16}$$

where we have left explicit the dependencies on our parametrizations.

4.4.2 *Radial density profile model $\propto {\rm r}^{-2}$ ($\Gamma = 2$)*

As a more realistic approach, here we try a density profile for the inter-cluster filaments with a core and that follows $n_{\rm H}(r) \propto r^{-2}$ at large distances as suggested by simulations (e.g. Aragón-Calvo et al. 2010)

$$n_{\rm H} = n_0 \frac{1}{1+\left(\frac{r}{r_{1/2}}\right)^2}. \tag{17}$$

Table 4. Characterization of each BLA. The errors associated with the redshifts in Column 2 are $\sim \pm 10\,\mathrm{km\,s^{-1}}$. The mean density $\overline{n_\mathrm{H}}$ was calculated for both scenarios proposed in Section 4.4 for all BLAs. Column 10 marks as 'n' the absorptions that are likely produced by WHIM according to Section 4.2

Parameters derived from BLAs									
ID	Redshift	b	Column densities		logf_ion	Temperature	Gas density		Has galaxy nearby?
							$\Gamma = 0$	$\Gamma = 2$	
		km s^{-1}	log($N_\mathrm{H\,I}$/cm^{-2})	log($N_\mathrm{H\,II}$/cm^{-2})		log(T/K)	log($\overline{n_\mathrm{H}}$/cm^{-3})		
(1)	(2)	(3)	(4)	(5)	(6)	(7)	(8)	(9)	(10)
1	0.1606	59±22	13.40±0.11	19.1±0.4	5.68±0.40	5.1±0.3	−6.2 ±0.4	−6.5 ±0.4	y
2	0.3422	153±19	13.75±0.05	20.5±0.1	6.72±0.13	6.0±0.1	−4.8 ±0.1	−5.1 ±0.1	n
3	0.3502	97±10	14.29±0.09	20.5±0.1	6.22±0.11	5.6±0.1	−4.8 ±0.1	−5.1 ±0.1	y
4	0.3689	50±18	13.25±0.11	18.8±0.4	5.50±0.39	5.0±0.3	−6.5 ±0.4	−6.8 ±0.4	n
5	0.4118	62±18	13.47±0.09	19.2±0.3	5.74±0.32	5.2±0.3	−6.1 ±0.3	−6.4 ±0.3	y
6	0.4202	56±20	13.25±0.12	18.9±0.4	5.63±0.39	5.1±0.3	−6.4 ±0.4	−6.7 ±0.4	y
7	0.4547	81±18	13.46±0.08	19.5±0.3	6.03±0.24	5.4±0.2	−5.8 ±0.3	−6.1 ±0.3	n

Assuming the same geometry as in the previous scenario, we integrate the density over a single sightline to calculate the core density n_0

$$n_0 = \frac{N_\mathrm{H}\gamma\cos(\theta)}{2r_{1/2}^2\tan^{-1}(a/\gamma)}, \tag{18}$$

where γ and a are geometrical parameters defined as follows:

$$\gamma \equiv R\sqrt{\epsilon^2 + \left(\frac{r_{1/2}}{R}\right)^2} \tag{19}$$

and

$$a \equiv R\sqrt{1-\epsilon^2} \tag{20}$$

and correspond to the typical size and typical core size of a filament. According to the results presented in Cautun et al. (2014), we use a value of $r_{1/2} = 2$ Mpc and integrate the density profile until it becomes approximately flat, i.e. at $R \approx 6$ Mpc. Using the three good WHIM candidate BLAs in our sample, we can calculate a typical core density $\overline{n_0}$ and average the density profiles over the transversal area of the filament to obtain the averaged mean particle density:

$$\langle\overline{n_\mathrm{H}}\rangle = \overline{n_0}\int_A \frac{1}{1+(\frac{r}{r_{1/2}})^2}\mathrm{d}A. \tag{21}$$

From this, and using our fiducial values of $a = 6$ Mpc and $\gamma = 2$ Mpc we obtained a value of:

$$\overline{n_0} = 7.1\times10^{-6}\left(\frac{\tan^{-1}(a/\gamma)}{1.25}\right)^{-1}\left(\frac{\cos(\theta)}{1}\right)\left(\frac{1+\alpha^2}{1.49}\right)^{-\frac{5}{4}}\mathrm{cm}^{-3} \tag{22}$$

for an average total integrated density of

$$\langle\overline{n_\mathrm{H}}\rangle = 2.9\times10^{-6}\left(\frac{\tan^{-1}(a/\gamma)}{1.25}\right)^{-1}\left(\frac{\cos(\theta)}{1}\right)\left(\frac{1+\alpha^2}{1.49}\right)^{-\frac{5}{4}}\mathrm{cm}^{-3}. \tag{23}$$

Table 4 summarizes the main findings adopting our fiducial values for the individual WHIM candidate BLAs. For completeness, in Table 4 we have also included the corresponding calculations for those BLAs that show nearby galaxies (marked with 'y' in the last column). Note that for the latter, the presence of nearby galaxies complicates the interpretation on its origin but does not necessarily rule out the possibility that these are genuine WHIM absorption. In fact we do not see an important quantitative difference in the inferred densities for good and uncertain WHIM candidates. We obtained a mean hydrogen particle density of $5.9 \pm 4.1 \times 10^{-6}\,\mathrm{cm}^{-3}$ in the uniform density scenario (Section 4.4.1) using the samples of BLAs that do not show nearby galaxies. If we use only the BLAs that could be potentially associated with a galaxy, we obtain a mean particle density of $4.9 \pm 4.2 \times 10^{-6}\,\mathrm{cm}^{-3}$. Similarly, in the radial density profile scenario we obtained a mean particle density of $2.9 \pm 2.0 \times 10^{-6}\,\mathrm{cm}^{-3}$ (Section 4.4.2). If we consider now the BLAs with uncertain origin only, we obtain a value of $2.4 \pm 2.1 \times 10^{-6}\,\mathrm{cm}^{-3}$.

5 DISCUSSION

5.1 The relation between BLAs and WHIM

Based on our blind MUSE survey, we have a first estimation of the fraction of BLAs in inter-cluster filaments that may represent genuine WHIM signatures based on the lack of nearby galaxies to stringent luminosity limits. We find this fraction to be ∼40 per cent (3/7). Despite an analysis of the luminosity function, we cannot rule out the presence of fainter or dust-enshrouded galaxies. How this number relates to BLAs discovered in blind absorption surveys is particularly relevant for observational studies focused on the WHIM. Although properly addressing this question is beyond the scope of this paper, we note that one could repeat the experiment presented here in non-targeted QSO sightlines and undertake an empirical comparison.

5.2 The baryon density in inter-cluster filaments

Here we provide an estimation of the implied baryon density in inter-cluster filaments, $\Omega_\mathrm{b}^\mathrm{fil}$. The results presented in Section 4.4 correspond to the typical volumetric densities implied by our three BLAs that are good WHIM candidates. In order to estimate the corresponding baryon density, we need to estimate the relative volume occupied by these large-scale filaments in the Universe v_fil. Thus,

$$\Omega_\mathrm{b}^\mathrm{fil} = \frac{8\pi G m_\mathrm{H}}{3H(z)^2(1-Y)}\langle\overline{n_\mathrm{H}}\rangle V_\mathrm{fil}, \tag{24}$$

where G is the gravitational constant, m_H is the hydrogen mass, $H(z)$ is the Hubble parameter, and Y is the baryonic mass fraction in helium. In the following we use a typical volume $V_\mathrm{fil} \sim 6$ per cent as inferred by cosmological simulations (e.g. Cautun et al. 2014). We note that this volume fraction may not be consistent with a uniform density model, given that such number comes from simulations

with a non-uniform density profile. Nevertheless, we have kept this number fixed as a fiducial value, but our results will be expressed explicitly on $v_{\rm fil}$.

5.2.1 *Uniform density model*

In the scenario of filaments with uniform density (see Section 4.4.1), assuming $\theta = 0$, $\epsilon = 0$, and $\alpha = 0.7$ as fiducial values, we estimated a mean gas particle density of $\langle \overline{n_{\rm H}} \rangle \approx 5.9 \times 10^{-6}\,{\rm cm}^{-3}$. According to equations (16) and (24) we have

$$\Omega_{\rm b}^{\rm fil} \approx 0.06 \left(\frac{\langle \overline{n_{\rm H}} \rangle}{5.9x10^{-6}{\rm cm}^{-3}} \right) \left(\frac{V_{\rm fil}}{0.06} \right) \left(\frac{1-Y}{0.76} \right)^{-1}, \quad (25)$$

giving us a value of $\Omega_{\rm b}^{\rm fil} \approx 0.06 \pm 0.04$, i.e. somewhat larger than the total baryon density expected $\Omega_{\rm bar} \approx 0.048$ (e.g. Planck Collaboration XIII 2016) but consistent within the errors. The error in these estimations comes from the standard error of the mean density of our sample.

With the aim at reducing the statistical uncertainties, here we also include the densities of the BLAs reported in Wakker et al. (2015). The authors reported a total of five BLAs, four of them in sightlines within 540 kpc to the axis of the filament and one of them at an impact parameter of ∼3 Mpc. We added these five BLAs to our sample, and calculated the corresponding $\langle \overline{n_{\rm H}} \rangle$ in the same manner as in Section 4.4. [7] Combining their and our sample of BLAs we obtain a somewhat better constrained value of $\Omega_{\rm b}^{\rm fil} \approx 0.04 \pm 0.02$.

5.2.2 *Radial density model* $\propto {\rm r}^{-2}$

Alternatively, in the scenario of a density profile $\propto r^{-2}$ (see Section 4.4.2) and using the same fiducial values for the main parameters as in the previous section, we estimated a mean gas peak density of $\overline{n_0} = 7.1 \times 10^{-6}\,{\rm cm}^{-3}$. By averaging the density profile over the transversal area of the filament, we obtained an overall mean gas particle density of $\langle \overline{n_{\rm H}} \rangle = 2.9 \times 10^{-6}\,{\rm cm}^{-3}$. Using equations (23) and (24) we obtain an alternative value for $\Omega_{\rm b}^{\rm fil}$ as

$$\Omega_{\rm b}^{\rm fil} \approx 0.03 \left(\frac{\langle \overline{n_{\rm H}} \rangle}{2.9x10^{-6}{\rm cm}^{-3}} \right) \left(\frac{V_{\rm fil}}{0.06} \right) \left(\frac{1-Y}{0.76} \right)^{-1}. \quad (26)$$

This new fiducial value $\Omega_{\rm b}^{\rm fil} \approx 0.03 \pm 0.02$ is somewhat lower than $\Omega_{\rm bar} \approx 0.048$, but subject to large statistical and systematic uncertainties. If we include in our sample the BLAs reported in Wakker et al. (2015) (see Section 5.2.1) we obtain a somewhat better constrained value of $\Omega_{\rm b}^{\rm fil} \approx 0.02 \pm 0.01$, consistent with expected value of $0.4 \times \Omega_{\rm bar} \approx 0.02$.

6 SUMMARY AND CONCLUSIONS

In this paper we used VLT/MUSE to perform a blind galaxy survey around a unique QSO whose sightline may be passing through seven inter-cluster filaments as presented in Tejos et al. (2016). In particular, we focus on the presence or lack of galaxies within $\Delta v = \pm 1000\,{\rm km\ s}^{-1}$ from each of the seven broad H I Lyα absorption (BLAs) found at these inter-cluster redshifts in order to determine their origin.

We detected 77 sources and characterized the redshift of 52 of them. We reached 100 per cent characterization completeness down to magnitude $r = 23$ mag, and ≈75 per cent completeness down to magnitude $r = 25$ mag. We found that four of the BLAs showed nearby galaxies, for which the origin of the BLAs is uncertain. These include a galaxy group at $z \approx 0.416$ and a potential galaxy halo BLA at $z \approx 0.35$ (not well constrained by the data, see Appendix E). On the other hand, we found three BLAs that do not show any galaxy nearby to stringent luminosity limits. The lack of a nearby galaxy implies that they may be produced by the long sought after WHIM, and would mean that a significant fraction (∼40 per cent) of the BLAs detected between cluster-pairs (where the existence of a filamentary structure can be expected) may be directly tracing WHIM.

Assuming these BLAs are genuinely produced by the WHIM, we estimated the mean gas particle density assuming two different density profile models for the filaments themselves. First, we used a uniform density profile scenario with a set of assumptions on the geometry and the broadening mechanisms involved, and estimated a rough mean gas density of $\langle \overline{n_{\rm H}} \rangle \sim (5.9 \pm 4.1) \times 10^{-6}\,{\rm cm}^{-3}$. This value implies an unrealistically large $\Omega_{\rm bar}^{\rm fil} \approx 0.06 \pm 0.04$, i.e. larger than the expected total baryon density of $\Omega_{\rm bar} \approx 0.048$ (Planck Collaboration XIII 2016) but still consistent within errors. In the second scenario, we assumed a radial density profile of the form $n_{\rm H}(r) \propto r^{-2}$ (as suggested by simulations; e.g. Aragón-Calvo et al. 2010), which led us to estimate a mean gas particle density of $\langle \overline{n_{\rm H}} \rangle \sim (2.9 \pm 2.0) \times 10^{-6}\,{\rm cm}^{-3}$ and a corresponding $\Omega_{\rm bar}^{\rm fil} \approx 0.03 \pm 0.02$. This value is similar to the expected $0.4\ \Omega_{\rm bar} \approx 0.02$ that may be in a WHIM state. Including the BLAs presented in Wakker et al. (2015) into our sample we obtain somewhat better constrained values for $\Omega_{\rm bar}^{\rm fil}$ of 0.04 ± 0.02 and 0.02 ± 0.01 for the uniform density and radial density model, respectively.

We emphasize that these estimations are subject to large statistical and systematic uncertainties, owing to our small sample of BLAs (3 and 3 + 5) and to the intrinsic uncertainties of our assumed geometrical parameters. Furthermore, the relationship between observed Doppler b parameters and gas-phase temperature is affected by poorly constrained physical processes (e.g. turbulence). The results presented here support the hypothesis that inter-cluster filaments host a significant amount of baryons, enough to close the baryon budget in the low-z Universe but larger samples need to be analysed for conclusive results.

ACKNOWLEDGEMENTS

Our results are based on observations collected at the European Organization for Astronomical Research in the Southern hemisphere under ESO programme 094.A-0575(C). Some of the data presented in this paper were obtained from the NASA/ESA Hubble Space Telescope under programme GO 12958, obtained at the Space Telescope Science Institute and from the Mikulski Archive for Space Telescopes (MAST). STScI is operated by the Association of Universities for Research in Astronomy, Inc., under NASA contract NAS5-26555. We thank the referee, John Stocke, for providing valuable comments and criticism that improved the paper. IP and NT acknowledge support from *CONICYT PAI/82140055.*

We thank contributors to SciPy, Matplotlib, Astropy (Astropy Collaboration et al. 2013), and the PYTHON programming language; the free and open-source community; and the NASA Astrophysics Data System for software and services. We also thank contributors to linetools (Prochaska et al. 2016) and PYMUSE (Pessa, Tejos & Moya 2018), both open-source PYTHON packages recently developed and used in this work.

[7] We note that the BLAs reported in Wakker et al. (2015) arise from the same filamentary structure instead of independent ones.

REFERENCES

Aragón-Calvo M. A., van de Weygaert R., Jones B. J. T., 2010, MNRAS, 408, 2163
Astropy Collaboration et al., 2013, A&A, 558, A33
Bacon R. et al., 2014, The Messenger, 157, 13
Bacon R., Piqueras L., Conseil S., Richard J., Shepherd M., 2016, Astrophysics Source Code Library, ascl:1611.003
Bertin E., Arnouts S., 1996, A&AS, 117, 393
Bonamente M., Nevalainen J., Tilton E., Liivamägi J., Tempel E., Heinämäki P., Fang T., 2016, MNRAS, 457, 4236
Borthakur S. et al., 2016, ApJ, 833, 259
Bruzual G., Charlot S., 2003, MNRAS, 344, 1000
Cautun M., van de Weygaert R., Jones B. J. T., Frenk C. S., 2014, MNRAS, 441, 2923
Cen R., Ostriker J. P., 1999, ApJ, 514, 1
Chabrier G., 2003, PASP, 115, 763
Cid Fernandes R., Mateus A., Sodré L., Stasińska G., Gomes J. M., 2005, MNRAS, 358, 363
Colberg J. M., Krughoff K. S., Connolly A. J., 2005, MNRAS, 359, 272
Coleman G. D., Wu C.-C., Weedman D. W., 1980, ApJS, 43, 393
Danforth C. W., Stocke J. T., Shull J. M., 2010, ApJ, 710, 613
Davé R. et al., 2001, ApJ, 552, 473
de Graaff A., Cai Y., Heymans C., Peacock J., 2017, preprint (arXiv:1709.10378)
Fang T., Bryan G. L., 2001, ApJ, 561, L31
Fang T., Croft R. A. C., Sanders W. T., Houck J., Davé R., Katz N., Weinberg D. H., Hernquist L., 2005, ApJ, 623, 612
Fukugita M., Hogan C. J., Peebles P. J. E., 1998, ApJ, 503, 518
González R. E., Padilla N. D., 2010, MNRAS, 407, 1449
Hattori S., Ota N., Zhang Y.-Y., Akamatsu H., Finoguenov A., 2017, PASJ, 69, 39
Hutchinson T. A. et al., 2016, AJ, 152, 205
Le Fèvre O. et al., 2005, A&A, 439, 845
Lehner N., Savage B. D., Richter P., Sembach K. R., Tripp T. M., Wakker B. P., 2007, ApJ, 658, 680
Li H. et al., 2017, ApJ, 838, 77
McNaught-Roberts T. et al., 2014, MNRAS, 445, 2125
Moster B. P., Somerville R. S., Maulbetsch C., van den Bosch F. C., Macciò A. V., Naab T., Oser L., 2010, ApJ, 710, 903
Penton S. V., Stocke J. T., Shull J. M., 2004, ApJS, 152, 29
Persic M., Salucci P., 1992, MNRAS, 258, 14p
Pessa I., Tejos N., Moya C., 2018, preprint (arXiv:1803.05005)
Planck Collaboration XIII 2016, A&A, 594, A13
Prochaska J. X., Tumlinson J., 2009, Astrophys. Space Sci. Proc., 10, 419
Prochaska J. X., Weiner B., Chen H.-W., Mulchaey J., Cooksey K., 2011, ApJ, 740, 91
Prochaska J. X., Tejos N., Crighton N., Burchett J.Tuo-Ji. 2016, linetools/linetools: Second major release, doi:10.5281/zenodo.168270
Rauch M., Haehnelt M. G., Steinmetz M., 1997, ApJ, 481, 601
Reed D. S., Bower R., Frenk C. S., Jenkins A., Theuns T., 2007, MNRAS, 374, 2
Richter P., Savage B. D., Tripp T. M., Sembach K. R., 2004, ApJS, 153, 165
Richter P., Fang T., Bryan G. L., 2006a, A&A, 451, 767
Richter P., Savage B. D., Sembach K. R., Tripp T. M., 2006b, A&A, 445, 827
Savage B. D. et al., 2014, ApJS, 212, 8
Sawala T. et al., 2016, MNRAS, 456, 85
SDSS Collaboration et al., 2016, ApJS, 233, 25
Shen L. et al., 2017, MNRAS, 472, 998
Shull J. M., Smith B. D., Danforth C. W., 2012, ApJ, 759, 23
Soto K. T., Lilly S. J., Bacon R., Richard J., Conseil S., 2016, MNRAS, 458, 3210
Stocke J. T. et al., 2014, ApJ, 791, 128
Sutherland R. S., Dopita M. A., 1993, ApJS, 88, 253
Tanimura H, Hinshaw G, Van Waerbeke L, Ma Y, Maed A, Hojjati A, Tröster T., 2017, preprint (arXiv:1709.05024)
Taylor E. N., 2011, MNRAS, 418, 1587
Tejos N. et al., 2016, MNRAS, 455, 2662
Tepper-García T., Richter P., Schaye J., Booth C. M., Dalla Vecchia C., Theuns T., 2012, MNRAS, 425, 1640
Tilton E. M., Danforth C. W., Shull J. M., Ross T. L., 2012, ApJ, 759, 112
Tripp T. M., Bowen D. V., Sembach K. R., Jenkins E. B., Savage B. D., Richter P., 2006, ASP Conf. Ser. Vol. 348, Astrophysics in the far ultraviolet: five years of discovery with FUSE. Astron. Soc. Pac., San Francisco, p. 341
Wakker B. P., Hernandez A. K., French D. M., Kim T.-S., Oppenheimer B. D., Savage B. D., 2015, ApJ, 814, 40
Weinberg D. H., Miralda-Escudé J., Hernquist L., Katz N., 1997, ApJ, 490, 564
Williams R. J., Mulchaey J. S., Kollmeier J. A., 2013, ApJ, 762, L10
Zucca E. et al., 2006, A&A, 455, 879

APPENDIX A: UNCHARACTERIZED SOURCES

Table A1 lists photometric sources identified in the MUSE data set but for which no redshift solution was found.

Table A1. List of the sources that could not be characterized. Sources where r is undefined were not detected by SEXTRACTOR and we manually included them in the survey.

Sources not characterized in our survey						
ID	Object	RA J2000	Dec. J2000	Impact parameter (arcsec)	r_{AB}	Reliability
(1)	(2)	(3)	(4)	(5)	(6)	(7)
1	J141038.12+230441.3	212.65883	23.07814	6.24	–	d
2	J141038.57+230440.7	212.66071	23.07797	6.42	24.27	d
3	J141038.54+230453.0	212.66058	23.08139	6.91	24.79	d
4	J141038.17+230435.9	212.65904	23.07664	10.95	25.36	d
5	J141037.60+230443.3	212.65667	23.07869	11.10	–	d
6	J141037.51+230445.8	212.65629	23.07939	11.89	24.57	d
7	J141039.24+230453.5	212.66350	23.08153	13.90	–	d
8	J141039.15+230456.4	212.66312	23.08233	14.62	–	d
9	J141038.38+230430.3	212.65992	23.07508	16.20	–	d
10	J141039.03+230430.7	212.66262	23.07519	18.24	24.21	d
11	J141038.55+230425.6	212.66062	23.07378	21.05	24.69	d
12	J141039.98+230454.5	212.66658	23.08181	23.61	–	d
13	J141037.24+230505.8	212.65517	23.08494	24.81	25.57	d
14	J141039.87+230425.6	212.66612	23.07378	29.42	27.38	d
15	J141036.36+230426.5	212.65150	23.07403	34.20	23.96	d
16	J141036.33+230507.5	212.65137	23.08542	35.12	–	d
17	J141036.65+230419.5	212.65271	23.07208	35.95	–	d
18	J141040.73+230508.3	212.66971	23.08564	39.19	24.96	d
19	J141038.38+230526.0	212.65992	23.09056	39.50	–	d
20	J141036.28+230418.2	212.65117	23.07172	40.41	–	d
21	J141041.09+230503.6	212.67121	23.08433	41.25	25.22	d
22	J141040.93+230508.3	212.67054	23.08564	41.51	26.30	d
23	J141037.52+230526.5	212.65633	23.09069	41.68	25.27	d
24	J141041.61+230437.6	212.67337	23.07711	45.59	25.17	d
25	J141039.53+230532.5	212.66471	23.09236	48.71	24.06	d

APPENDIX B: *K*-CORRECTION

We have calculated the photometric K-correction in the r filter for galaxies in our survey as follows. We used empirical templates presented in Coleman, Wu & Weedman (1980) extended to blue wavelengths according to Bruzual & Charlot (2003) models to calculate the predicted $r - i$ colour and observed r_{AB} at different redshifts for different spectral types from E to Im. We obtained a monotonic relation between $r - i$ colour and K-correction for each redshift bin. We then empirically calculated the $r - i$ colour for the galaxies in our survey with known redshifts and interpolated this relation to obtain their corresponding K-correction.

APPENDIX C: SDSS GALAXIES

Table C1 lists SDSS spectroscopic galaxies from the SDSS outside our MUSE FoV up to impact parameters of ≈500 kpc.

Table C1. List of the SDSS spectroscopic galaxies outside the MUSE FoV and within 500 kpc from the QSO sightline.

SDSS spectroscopic galaxies				
Object		r	Impact parameter	z
RA	Dec.		kpc	
14:10:33.00	+23:05:44.87	17.04	264	0.1579
14:10:46.43	+23:02:49.87	17.12	456	0.1584
14:10:50.97	+23:05:13.20	16.72	494	0.1580

APPENDIX D: REDMONSTER REDSHIFTS MEASUREMENTS

Figs D1–D7 show the spectra of identified sources in the MUSE data that were characterized using REDMONSTER software.

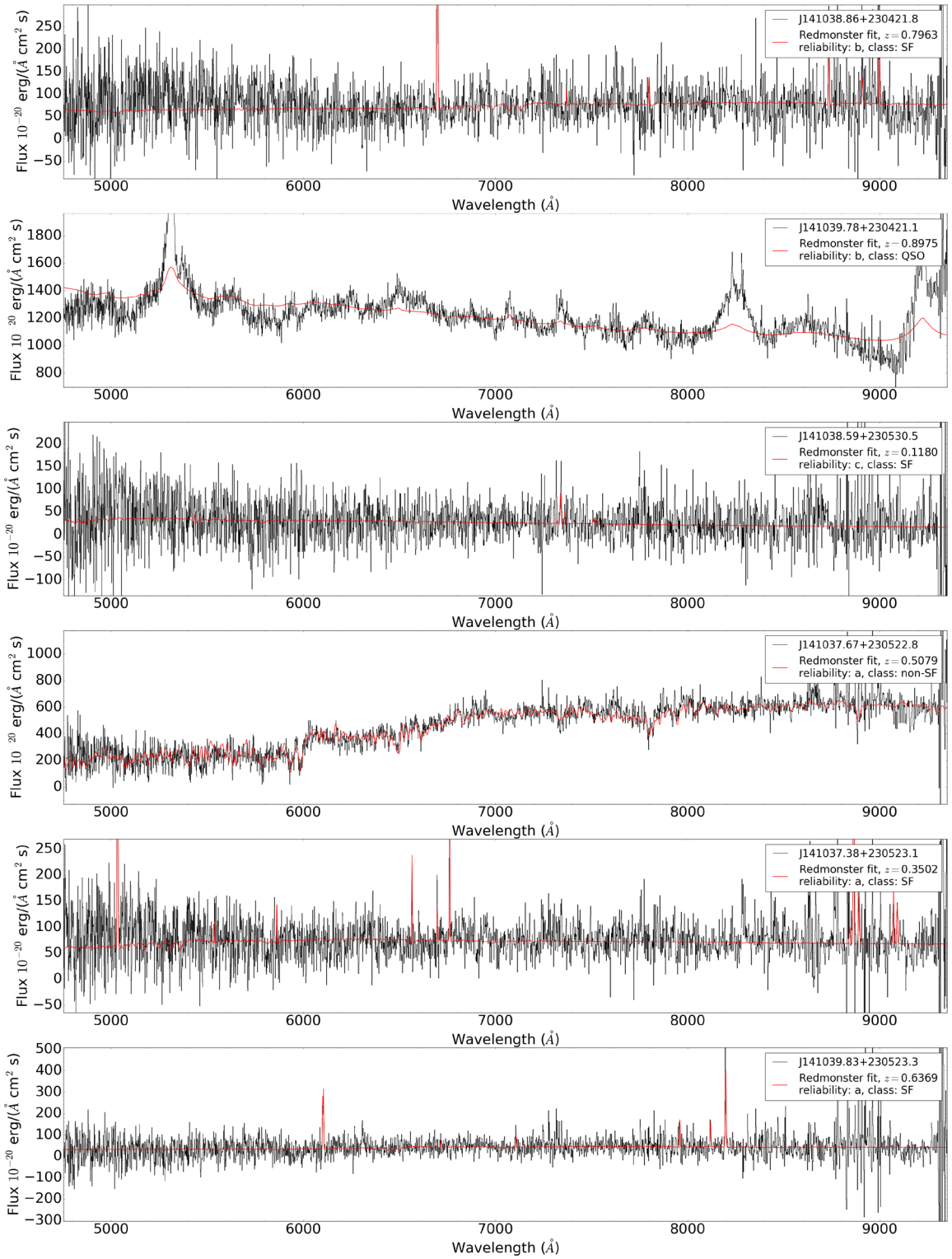

Figure D1. Spectra characterized using REDMONSTER software.

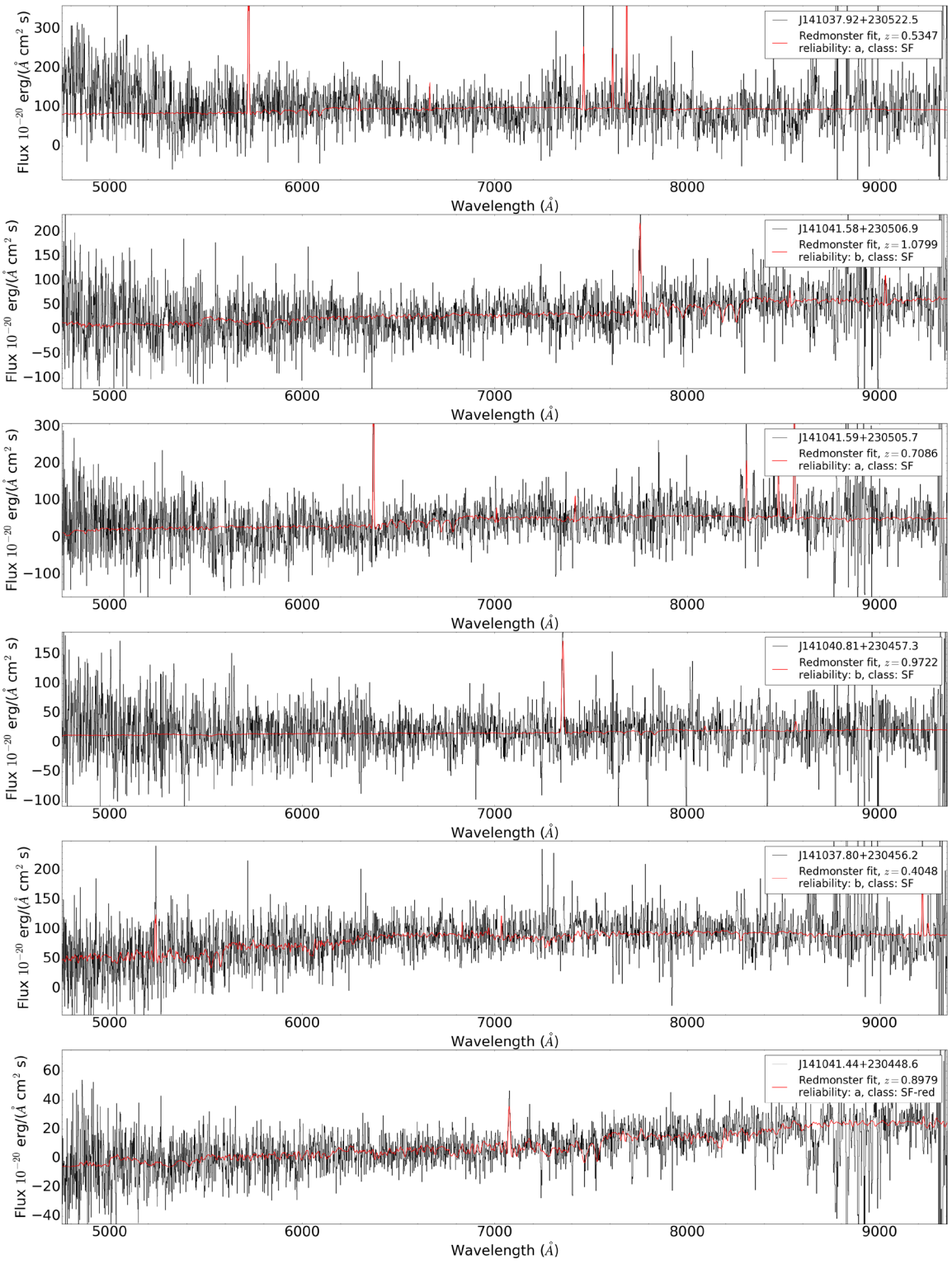

Figure D2. Spectra characterized using REDMONSTER software.

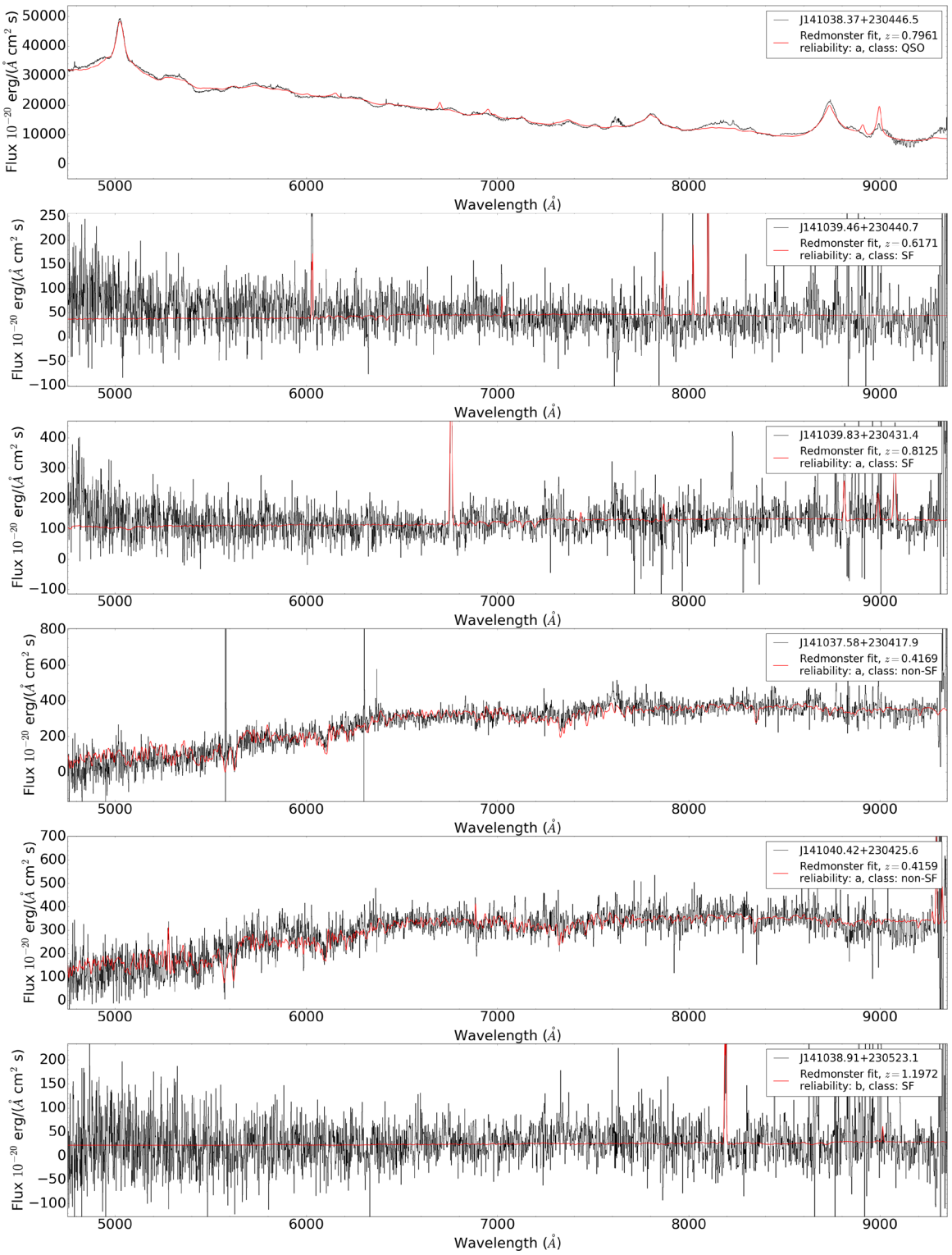

Figure D3. Spectra characterized using REDMONSTER software.

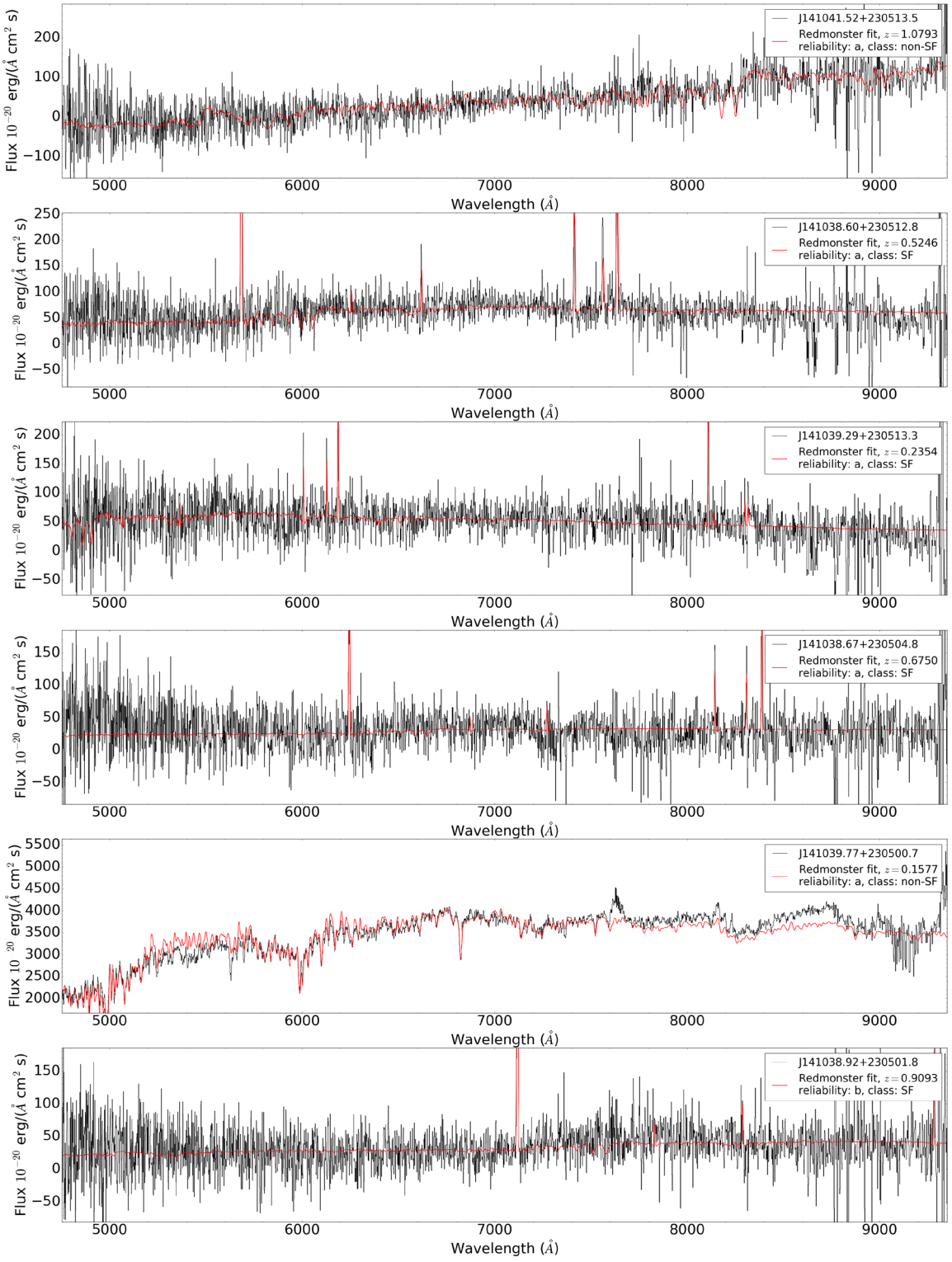

Figure D4. Spectra characterized using REDMONSTER software.

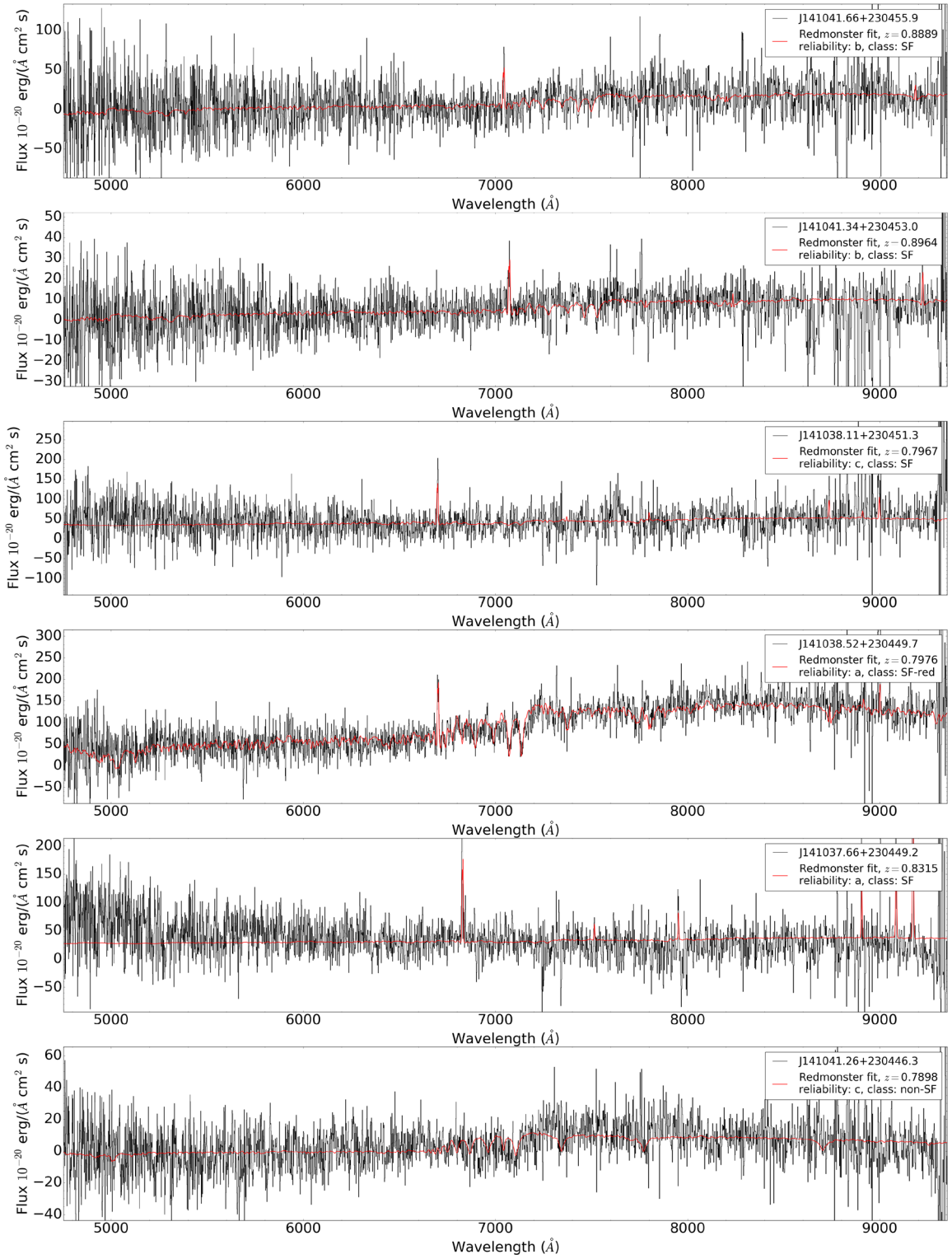

Figure D5. Spectra characterized using REDMONSTER software.

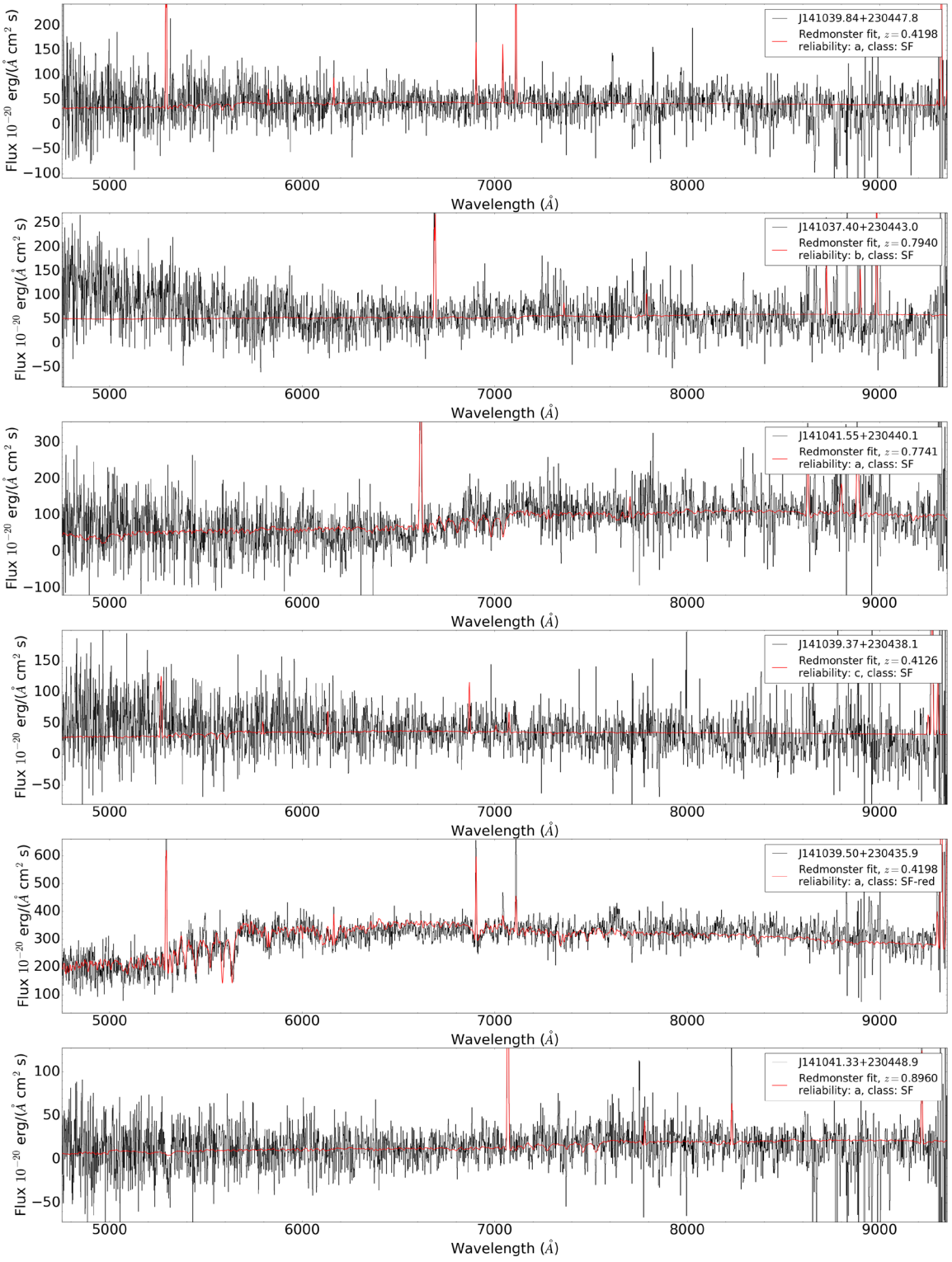

Figure D6. Spectra characterized using REDMONSTER software.

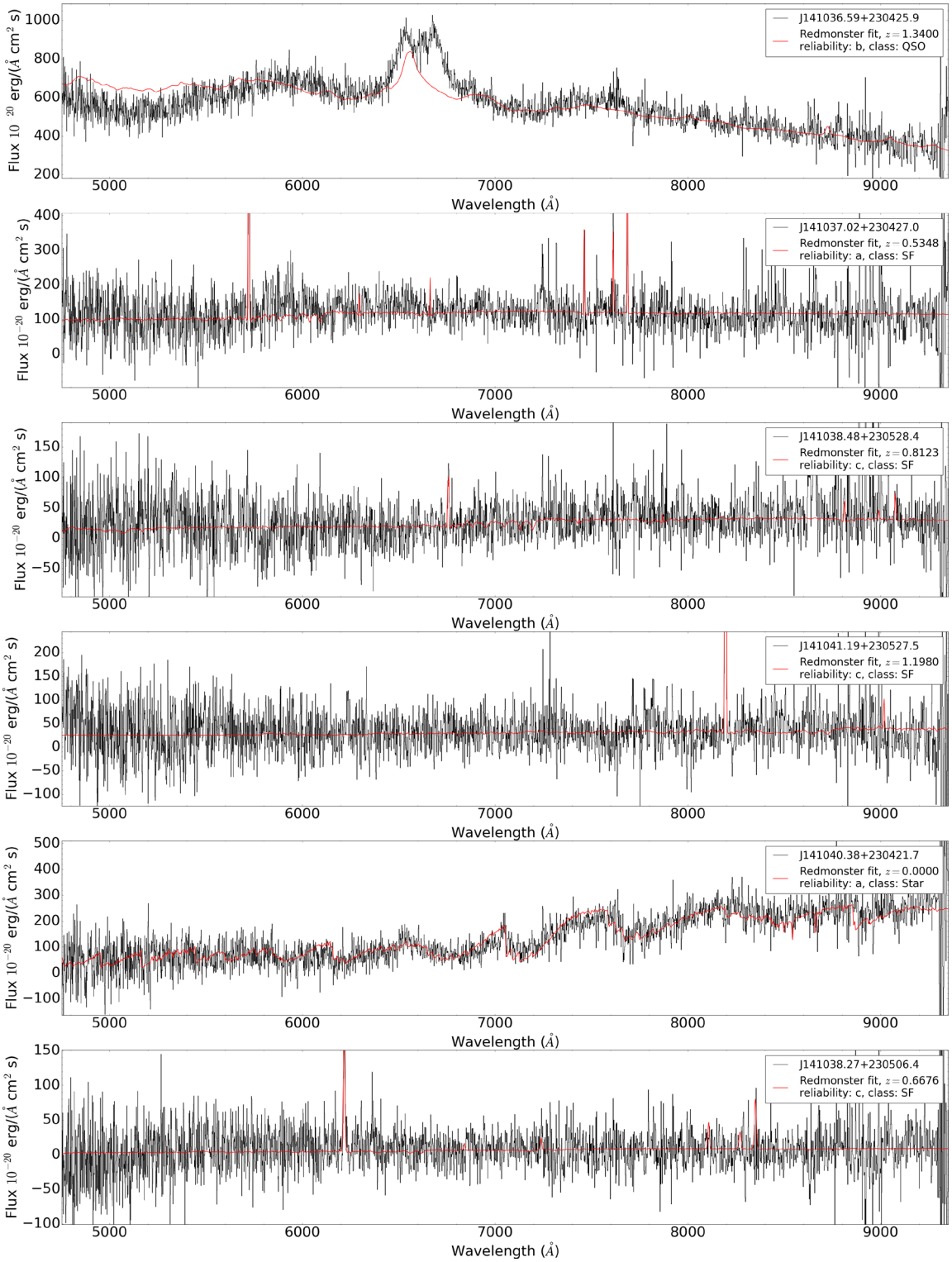

Figure D7. Spectra characterized using REDMONSTER software.

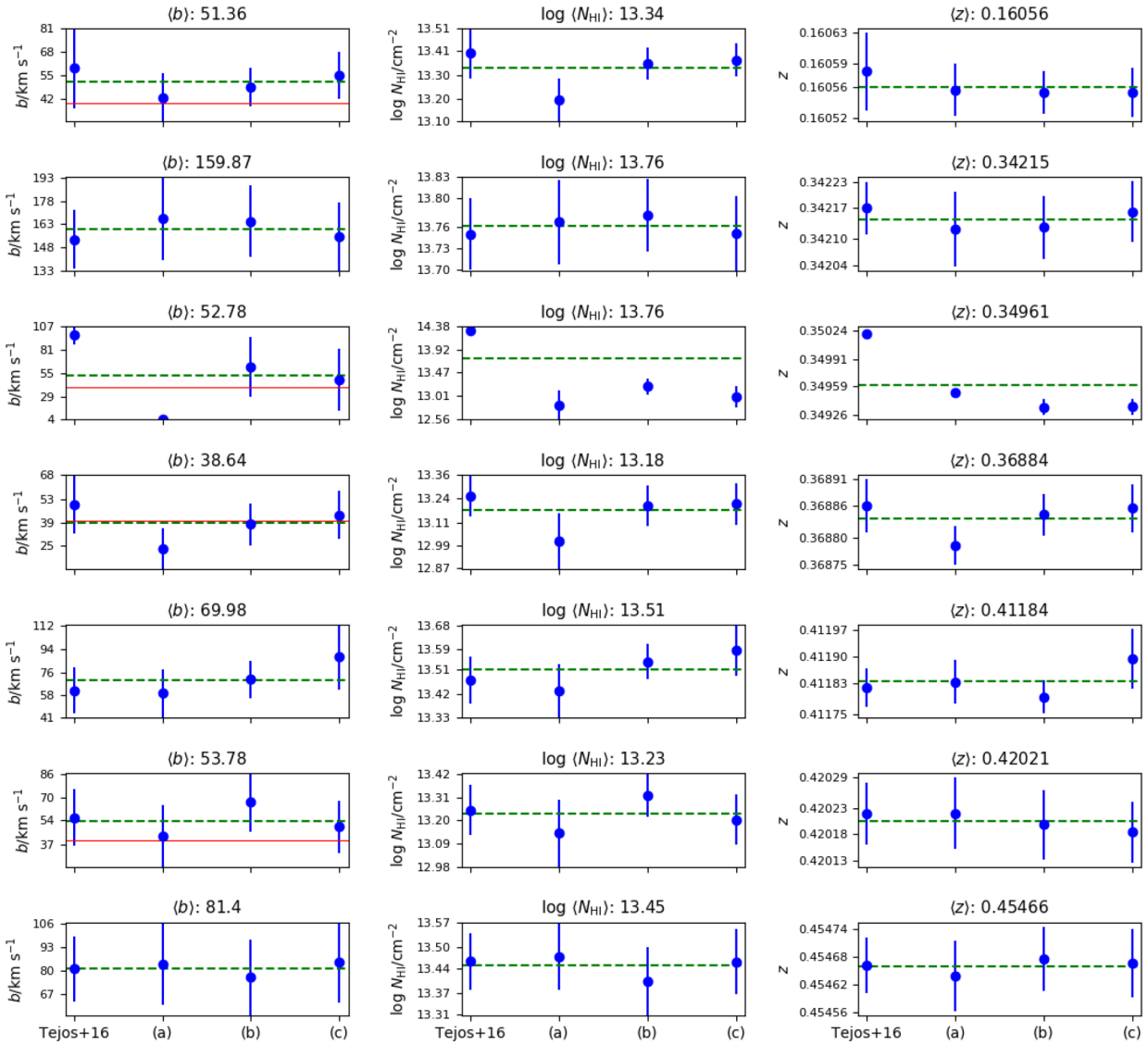

Figure E1. Systematic comparison between the parameters obtained for the BLAs in our sample using a different data reduction, an independent continuum level estimation, and a different Voigt profile fitting software. (a), (b), and (c) represent different combination of these variables with respect to those used in Tejos et al. (2016). With the exception of the absorption feature at $z = 0.3502$, all absorption features have systematic variations consistent with the level of reported statistical uncertainties. More details are given in Section 4.3.

APPENDIX E: RE-ANALYSIS OF BLAS REPORTED BY TEJOS ET AL. (2016)

In order to test for potential systematic errors in the characterization of BLAs by Tejos et al. (2016), here we have revisited their identifications and fit parameters. In particular, we repeated their analyses using the following:

(i) *Different data reduction* For our comparison we used the reduced Q1410 *HST*/COS data provided by the MAST *HST* archive[8] (referred to as 'new data') as opposed to the custom reduction done by Tejos et al. (2016, referred to as 'old data'). We note that the 'old data' have slightly higher signal-to-noise ratio than the 'new data'.

(ii) *Different continuum level estimation* For our comparison we used an independent estimation of the continuum level obtained from the 'new data' (referred to as 'new continuum') as opposed to the old continuum estimation described by Tejos et al. (2016, referred to as 'old continuum').

(iii) *Different Voigt profile fitting software* For our comparison we used VEEPER[9] as opposed to VPFIT[10] used by Tejos et al. (2016).

From the above, we performed the following combinations to define a set of new experiments: (a) new data and new continuum, (b) old data and new continuum, and (c) old data and old continuum, all of which performed using the new software VEEPER. Fig. E1 shows the obtained parameters for the putative BLAs from our different experiments and how these compare to those reported by Tejos et al. (2016). We see that, with the exception of the absorption feature at

[8] https://archive.stsci.edu/hst/

[9] Mainly developed by J. Burchett; available at https://github.com/jnburchett/veeper.

[10] Developed by R.F.Carswell and J.K.Webb; available at http://www.ast.cam.ac.uk/~rfc/vpfit.html.

$z = 0.3502$, all absorption features have systematic variations well below (or consistent with) the level of reported statistical uncertainties. The putative BLA at $z = 0.3502$ is the less constrained one as it may be superimposed to a complex narrow H I system and its absorption profile is degenerate with that of the narrow component. Indeed, in experiment (a) this absorption feature was fitted with a very narrow line (Doppler parameter $b < 10\,\mathrm{km\,s^{-1}}$) casting doubt on it being a genuine BLA. In any case, this feature has been also excluded from our 'clean BLA sample' (for the estimation of the filament baryon fraction in Section 5.2) on the basis of the existence of a potential galaxy counterpart (see Section 4.2).

This paper has been typeset from a TEX/LATEX file prepared by the author.